Chemical Engineering Journal 532 (2026) 174416

Contents lists available at ScienceDirect

Chemical Engineering Journal

journal homepage: www.elsevier.com/locate/cej

Triboelectric performance and delayed charge generation in triglyceride–sulfur synthesized from waste sources

Petr Slobodian [a,b], Berenika Hausnerova [b,c,*], Cesar Alfredo Barbero [a,d], Pavel Riha [a,b]

[a] Department of Physics and Materials Engineering, Tomas Bata University in Zlin, Vavreckova 5669, 760 01, Zlin, Czech Republic
[b] Centre of Polymer Systems, University Institute, Tomas Bata University, Trida T. Bati 5678, 76001, Zlin, Czech Republic
[c] Department of Production Engineering, Faculty of Technology, Tomas Bata University in Zlin, Vavreckova 5669, 760 01, Zlin, Czech Republic
[d] Chemistry Department, National University of Rio Cuarto, Ruta Nacional 36-km, 601-5800, Rio Cuarto, Argentina

ARTICLE INFO

Keywords:
Sulfur-triglyceride thermoplastic film
Inverse vulcanization
Triboelectric nanogenerator
Tribo-negative surface
Delayed charge
Sustainable energy material

ABSTRACT

Sulfur–triglyceride (STG) was synthesized by solvent-free inverse vulcanization of elemental sulfur and waste soybean frying oil and processed by compression molding into flexible 0.5 mm thermoplastic film. The resulting sulfur-rich polymer shows a robust, tribo-negative surface (confirmed by Kelvin Probe AFM and the position in Triboelectric Charge Density series) and was implemented as the negative layer in a vertical contact–separation triboelectric nanogenerator (TENG) operated against stainless steel and selected wearable-relevant counter materials. Under cyclic loading the STG-based TENG exhibits progressive charge accumulation with output stabilization, reaching peak open-circuit voltages up to ~570 V and maximum power densities of ~4.05 $mWcm^{-2}$ (STG/steel, ~1 MΩ, 14.8 kPa) and ~ 4.9 $mWcm^{-2}$ (STG/PVAc, ~2.2 MΩ, 14.8 kPa). Systematic parametric tests related to various mechanical pressures, resistive loads, actuation frequencies and contact areas are provided. Device durability was verified by long-term cycling tests up to 10^5 actuation cycles, demonstrating stable operation without STG degradation. Beyond cyclic loading, post-separation experiments reveal a delayed voltage generation associated with interfacial polarization and charge retention. The results demonstrate that waste-derived STG is a sustainable tribo-negative material providing pressure-, frequency-, and area-dependent power output together with a delayed-charge response associated with interfacial polarization.

1. Introduction

An interest in sustainable materials, which reduce environmental impact and promote resource efficiency, has grown significantly in recent years. This approach emphasizes reuse and recycling of industrial by-products by converting residues into valuable resources to create functional materials of high added value. The utilization of traditionally considered low-value materials as an elemental sulfur and triglycerides from waste vegetable oils, is presented. The research focuses on the development of so called high-sulfur-content materials [1–16] with sustainable properties focused on processing methods which avoid organic solvents and chemical initiators. Instead, in this work, a sulfur-triglyceride (STG) polymer is prepared by reacting of unsaturated triglyceride-based oils with excess of elemental sulfur via inverse vulcanization, resulting in a crosslinked network.

Sulfur is produced in large quantities as a by-product of petro-chemical industry [1–3], for example, in oil refining, fossil fuel processing, or natural gas desulfurization. This overproduction poses both environmental and logistic challenges due to a need for a long-term storage and risk of environmental impacts such as contamination of water resources or emissions from combustion. Although specialized applications, e.g. in the field of advanced functional materials, do not significantly affect overall consumption volumes, they represent an important direction for the use of sulfur with added value in the circular economy.

Waste oils and fats, such as unsaturated triglycerides from used vegetable oils [4] or animal fats such as rancid chicken fat [5], are also considered as low-value residues. However, in the context of this research, they represent a valuable source of an organic monomer. For example, sunflower oil [5] and rapeseed oil are triglycerides, esters of glycerol and fatty acids, and serve as renewable raw materials [4,6,7] similar to palm oil [8]. Furthermore, unsaturated fatty acids such as oleic and linoleic acid [3] and other unsaturated compounds with a carbon–carbon double bond such as limonene [9], olefins [10], 1,3-

* Corresponding author at: Centre of Polymer Systems, University Institute, Tomas Bata University, Trida T. Bati 5678, 76001, Zlin, Czech Republic.
E-mail address: hausnerova@utb.cz (B. Hausnerova).

https://doi.org/10.1016/j.cej.2026.174416
Received 8 October 2025; Received in revised form 15 February 2026; Accepted 19 February 2026
Available online 20 February 2026

diisopropenylbenzene [11,12], and 4-methyl-5-vinylthiazole [13] can be used.

STG product is formed via inverse vulcanization [1–3]. During the reaction, sulfur simultaneously acts as a solvent, initiator and monomer [1,2]. When heated above 159 °C, it undergoes transformation into biradical species which allow polymerization with unsaturated compounds without need of additional initiators or solvents [1,10]. The result is a cross-linked polysulfide network consisting of S—S bonds formed by polymerization of elemental sulfur and C—S bonds formed by reaction with carbon–carbon double bonds in the organic comonomer. This covalently cross-linked network contributes to the unique chemical, thermal, and mechanical properties of the final material.

Such sulfur-based materials exhibit exceptional thermal stability [5,8,16], high compressive strength [5,15], reduced flammability [16], and excellent acid resistance [15]. They are generally amorphous [1], and thus they can be molded above their softening temperature and reused [7,14] as functional components. Another advantage is their self-healing ability enabled by dynamic disulfide (S—S) bonds [11]. Current research highlights their potential in various areas, including the use as the cathode materials for lithium–sulfur batteries [12,13,15], energy generation and storage, and photocatalytic water splitting [2]. Their hydrophobic nature and strong affinity for hydrocarbons make them effective in separating oil contaminants from seawater [4]. Polysulfides also exhibit strong adsorption capacity for heavy metals removal [8,13,15] with particularly high affinity for mercury, palladium, and gold [1].

Sulfur-rich polymers, which combine high sulfur content with dynamic disulfide bonds, have recently been recognized as promising candidates for an energy harvesting through triboelectric nanogenerators (TENGs) [17]. Combined with an electrostatic induction, a triboelectric mechanism allows the TENG to convert mechanical energy into electric. TENGs, which operate on the principle of the contact electrification, are rapidly developing in the fields of energy harvesting and powering self-sustained electronic systems [18,19] due to their simple design and low-cost fabrication.

Currently, halogenated polymers such as polytetrafluorethylene (PTFE) [20] and polyvinylidenfluoride (PVDF) [20,21] are commonly used to achieve high triboelectric polarization, because of their high electron affinity, and thus an effective electron acceptance. However, in order to minimize environmental risks associated with the release of poly- and perfluoroalkyl substances from fluorinated polymers, other polymers including recycled and waste-derived plastics are presently developed to promote resource efficiency. For example, a TENG was successfully fabricated using discarded cigarette filters as the positive triboelectric layer and recycled plastic waste (polyethylene terephthalate (PET), polyprophylene (PP), polyvinyl chloride (PVC), and PTFE) as the negative layer [22]. Similarly, waste polystyrene (PS) from packaging materials combined with discarded PTFE tape was used to construct a high-performance TENG with strong environmental credentials [23]. Another study demonstrated a TENG using waste plastic bags and PTFE film in a vertical contact-separation configuration [24]. In a comparable approach, biaxially oriented PET films obtained from post-consumer food packaging were shown to exhibit both triboelectric and pressure-induced behavior, enabling their application in hybrid nanogenerators [25,26]. In addition, immiscible blends of common waste polymers such as high-density polyethylene (HDPE), PP, PS, and PET can form multiphase domain structures which enhance their triboelectric responses [27,28].

The inorganic polymers, formed by the reaction of elemental sulfur with organic cross-linkers, show strong potential for an efficient accumulation of negative charge during triboelectric separation due to high electronegativity of sulfur. In the recent study, a fluorinated sulfur-based polymer was synthesized using fluorine gas, which combines the triboelectric advantage of halogenation with the unique properties of the sulfur backbone. The open-circuit voltage of the resulting TENG reached 1366 V enabling direct powering of 630 LEDs with a minimum applied force of approximately 30 N [29]. As a safer alternative to a direct fluorination, a following study used a fluorinated compound, poly (2,3,4,5,6-pentafluorostyrene) (PPFS), which was physically blended during the inverse vulcanization of an elemental sulfur. During a subsequent hot pressing, the hydrophobic PPFS underwent phase separation and migrated to the film surface, where it formed fluorinated interface with enhanced triboelectric negativity. The TENG device containing 7.5 wt% PPFS achieved a power density of 116 mWm^{-2} and an open-circuit voltage of 164 V. When the active area was increased to 81 cm^2, the device generated 1362 V, and successfully powered 400

Table 1
Benchmarking of waste-based TENGS comparing open-circuit voltage Voc, short circuit current Isc, power P, power density PD, operating force F, frequency f, devise area A, electrode material and testing mode.

Waste	Pair	*Voc* V	*Isc* μA	*P* mW	*PD* mW/cm²	Mode	Stability	*f* Hz	*F* N	*A* cm²	Elect.
soybean meal [35]	soybean film	28	0.08	—	—	CS	—	—	—	6.25	Al
sea shells (SS) [36]	SS/Silicone	200	40	—	0.095	VCS	10000	3-4	~7	25	Al
peanut shell (PS) [37]	PS/PET	390	14	1.3	—	CS	6000	10	—	22.5	Al
rice husk (RH) [38]	RH-PDMS/PTFE	190	1	0.059	0.012	CS	—	—	—	5	Cu
cotton (MCC) [39]	MCC-PVA/Kapton	600	50	0.338	8.45	VCS	10000	5	4-5	4	Al
surgical mask [40]	PP/BOPET	200	—	—	0.071	CS	10000	3	3	6	Cu
saline bottles [41]	PE/Silicone	508	105	—	8.78	VCS	10000	4	—	25	Al
laboratory [42]	glass/PET	185	1.25	—	0.008	VCS	~4000	0.5-2	—	—	Al
expired drugs [43]	guaifenesin/PET	561	53	1.96	0.163	CS	20000	10	—	12	Al
X-ray film [44]	X-Ray	201	63	—	0.139	VCS	10000	4	4-10	25	—
post-consumer plastics (PCP) [27]	PCP/PET	130	312	—	2.6	VCS	1000	1	—	6.25	Cu
wooden plastics (WPC) [45]	WPC/PTFE	31	30	—	0.011	CS	5 000	4	—	25	Al
soda can [46]	coated Al/PET	519	82	12.25	0.51	CS	72 000	10	—	24	Al
LCD display [47]	LCD/FEP	470	143	—	0.504	VCS	6000	5-6	—	25	Al
OPC drum [48]	OPC/FEP	492	138	—	0.461	VCS	10000	5-6		25	Al

Note: in *green* – bio, *red* – medical, *yellow* – household, *blue* – electrical waste material.

series-connected blue LEDs [30].

To further enhance TENGs performance, a high sulfur composite with MXene nanosheets was developed. MXene, added in a low concentration (< 0.5 wt%), created the segregated structure in the polymer matrix, thereby increasing a dielectric constant without electrical percolation or significant increase in a dielectric loss. The resulting TENG device exhibited an open-circuit voltage of 331 V, and a power density of 810 mWm^{-2} [31]. A recent review further highlights the role of high sulfur materials in a diverse energy field and optical applications [32].

To place our waste-derived STG in a broader sustainability context we refer to the recent comprehensive reviews by Basith et al. [33] and Kumar et al. [34]. Table 1 summarizes representative examples of triboelectric materials prepared from different waste streams (biowaste, medical, electronic, packaging and household), highlighting that comparable or even higher performance than conventional polymer systems can be achieved from low-value residues [35–48]. As can be seen from Table 1, most waste-based TENG devices show moderate outputs, but their direct comparison is complicated by differences in experimental conditions, as well as by inconsistent reporting data, including stability tests. In this work, we investigate the potential for triboelectric energy harvesting of a sulfur-triglyceride (STG) polymer prepared by solvent-free inverse vulcanization of an elemental sulfur with unsaturated triglycerides obtained from waste oils. The combination of a waste-derived sulfur–triglyceride backbone with an intrinsically hydrophobic, non-porous surface distinguishes this TENG from many bio-waste systems. We focus on the synthesis and characterization of STG-based films, and systematically evaluate their triboelectric performance under cyclic mechanical excitation. In addition, we investigate how variations in test conditions, particularly applied pressure, frequency, resistive load, and contact area affect the output voltages. The aim of this study is to demonstrate the viability of STG films as sustainable, low-cost materials for triboelectric nanogenerators.

2. Experimental

2.1. Materials

The sulfur used in this study was an orthorhombic yellow powder, a residue of the desulphurization of oil and gas, and the oil was a commercially available soybean frying oil. STG – a sulfur–triglyceride polymer – was synthesized by inverse vulcanization, where heating above 159 °C led to ring opening of sulfur (S_8) and formation of sulfur radicals reacting with C═C double bonds in unsaturated triglycerides to form a chemically crosslinked copolymer with S—S and C—S bonds.

Elemental sulfur (30 g) was heated to 160 °C in a 500 mL stirred batch reactor until molten. The oil was then introduced (oil:sulfur = 20:80 wt%) under stirring (90 rpm); after ~5 min the two phases merged into a single homogeneous melt. The temperature was raised to

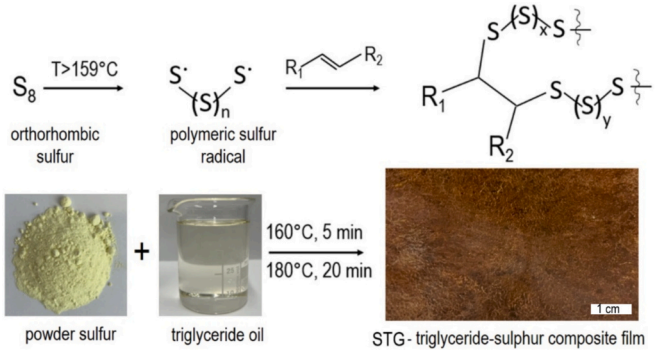

Fig. 1. Synthesis and processing of sulfur-triglyceride, and micrograph of resulting compression molded film.

180 °C, and after about 20 min the viscosity increased sharply. Stirring was stopped, and the material was allowed to cool to a room temperature, yielding a reddish-brown solid that was ground to powder in a blade mill.

For subsequent analyses and triboelectric measurements, the sulfur–triglyceride polymer was processed into flexible films by compression molding at 120 °C for 5 min. A PTFE-coated fiberglass release film prevented adhesion and imparted its surface texture to the molded sheets. The resulting STG films were ~ 0.5 mm thick. Their thermoplastic character enabled deformation under heat and pressure, facilitating formation of uniform films suitable for a triboelectric testing. A schematic overview of synthesis, polymerization mechanism, and film preparation is shown in Fig. 1.

A scanning electron microscope (SEM, NOVA NanoSEM 450 from FEI Co., Hillsboro, OR, USA) operating at an accelerating voltage of 10 kV, was used to analyze the cross-section of the sulfur-triglyceride film fractured after cooling in a liquid nitrogen. During Energy Dispersive X-ray Spectroscopy (EDS) data collection, each point was scanned 10 times, and the data were converted to the quantification maps with a resolution of 128 × 128 pixels. The analysis detects elements in concentrations higher than 0.1%. The surface of the STG film was characterized with surface roughness parameters (the arithmetic mean height Sa, the root mean square height Sq; and the maximum height Sz according to the ISO 21920-2 standard (2023)) using a 3D scanner (Zygo NewView 8000, AMETEK, Inc., Middlefield, Connecticut, USA) with a coherence scanning interferometry (CSI) technology, which combines VSI – vertical scanning interferometry and PSI - phase shifting interferometry.

Surface potential measurements were performed using amplitude-modulation Kelvin probe force microscopy (AM-KPFM) on an atomic force microscope (Dimension Icon, Bruker, Santa Barbara, California, USA) at room temperature in air. A Pt—Ir coated probe with a resonant frequency of 75 kHz and a stiffness constant of 3 N/m (SCM PIT V2, Bruker, Santa Barbara, California, USA) was used.

X-ray photoelectron spectroscopy (XPS) analyses were performed on XPS spectrometer (Genesis, Physical Electronics ULVAC, Chanhassen, Minesotta, USA), equipped with an Al monochromatic source. The analyzed area was 0.1 mm in diameter. A low-energy electron flood gun and a low-energy Ar-ion beam were used during measurements to reduce charging.

Fourier transform infrared spectroscopy (FT-IR) was employed to characterize soybean oil and inverse vulcanization product, verifying the occurrence of the expected chemical reaction and the formation of covalent bonds such as S—S and S—C. FT-IR spectra were recorded using a Thermo Scientific Nicolet iS50 FT-IR spectrometer with an attenuated total reflectance (ATR) module, covering the spectral range from 4000 to 400 cm^{-1} at a resolution of 4 cm^{-1}. X-ray diffraction (XRD) analysis was performed to determine the crystalline modifications of sulfur in the STG. The measurements were carried out using a MiniFlex™ diffractometer (Malvern Panalytical, Malvern, UK) with CoKβ radiation at 40 kV and 15 mA. The sample was scanned over a 2θ range of 10–90°, and the collected data, originally obtained using a cobalt source, were subsequently converted to a copper source using PowDLL software.

Differential scanning calorimetry (DSC, Perkin Elmer, Waltham, MA, USA) was performed to analyze the thermal properties of initial materials and STG. The primary objective was to determine the transformation temperatures associated with a solid-to-liquid phase transition as the melting temperatures characterizing the differences between reactants and the final STG product, and also to find a suitable temperature for STG compression molding with an assessment of its thermoplastic properties in the molten or softened state. The first scan for all samples was performed from −90 °C to 190 °C at a heating rate of 10 °C/min with a sample weight of 10 mg measured in a N_2 atmosphere at a rate of 20 ml/min. The second scan was performed by holding a sample at 190 °C for 5 min, followed by cooling to −90 °C, stabilization for 1 min at −90 °C, and then heating from −90 °C to 190 °C at a rate of

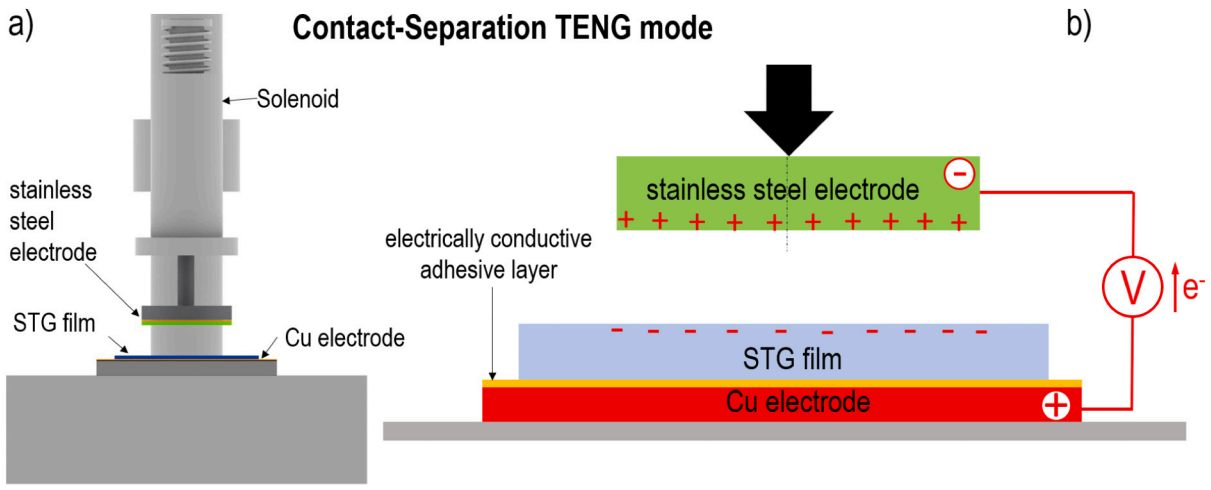

Fig. 2. Experimental setup for contact–separation triboelectrification using a solenoid actuator (a), and schematic illustration of TENG principle based on triboelectric charge generation and interfacial processes (b).

10 °C/min.

Dielectric analysis (DEA) of STG was performed to determine the frequency-dependent relative permittivity and dielectric loss of the STG film. The measurements were performed using a broadband dielectric/impedance analyzer (Novocontrol Technologies GmbH & Co. KG, Montabaur, Germany). The STG sample of 0.5 mm thickness was placed between two gold-plated electrodes with a diameter of 20 mm and tested in the frequency range from 1 Hz to 1 MHz at a room temperature. The relative permittivity (ε') was evaluated to assess the material's ability to store electrical energy, while the dielectric loss (tan δ) provided insight into the dissipative behavior of the composite.

Mechanical properties of the STG films were evaluated to demonstrate that the material, synthesized by inverse vulcanization from initially powdered sulfur and liquid oil, forms a solid product with mechanical integrity and usable stiffness. The tests were performed on STG film samples with a thickness of 0.5 mm, a width of 10 mm, and a length of 40 mm, using a tensile testing machine (M350-5CT, Tensometric, Manchester, UK) in a uniaxial extension mode. The samples were stretched at a constant rate of 10 mm/min to obtain stress–strain curves.

2.2. Triboelectric measurement and energy harvesting

The triboelectric properties and energy harvesting potential of the STG were analyzed using a contact-separation mode triboelectric nanogenerator (TENG). This experimental configuration allows for controlled cyclic contact-separation facilitating the evaluation of charge transfer and charge accumulation. A schematic representation of the setup is shown in Fig. 2 illustrating the functional components and operating principle of the TENG. Fig. 2a illustrates TENG, where a solenoid-driven mechanic system enables cyclic contact and separation. The principle is shown in Fig. 2b, where upper electrode consists of steel cylinder with a very smooth surface that repeatedly impacts and separates from the STG film (40 × 40 mm). An electrically conductive adhesive layer between the STG film and the lower copper electrode ensures efficient charge transfer. Fixing the STG film on the Cu electrode eliminates parasitic phenomena, such as friction between the layer and the electrode surface [49].

Dielectric polarization and electrostatic induction during the contact–separation process induce a potential difference between the electrodes, which controls the redistribution of the charges through the external circuit, and result in a measurable voltage (transferred charge) that reflects the combined effect of STG polarization and dynamic processes at the interface. The charge transfer through the external circuit between the electrodes can begin as soon as the surfaces approach each other due to electrostatic induction effects [50].

The application of the periodic mechanical contact and separation with the reversible linear solenoid was precisely controlled by an Arduino hardware. Each cycle consisted of one impact every 2 s with approximately 1 s of contact time followed by a separation. The resulting mechanical pressure acting on the STG was measured using a strain gauge powered by an analog converter (TZA11410, VTS Zlin s.r.o., Zlin, Czech Republic) with an output of ±20 mA and a 24 V DC power supply. The mechanical parameters used in the triboelectric measurements are summarized in Table 2.

The impact conditions were modulated by adjusting the DC control voltage applied to the solenoid actuator, which directly affected both the contact pressure and the impact velocity. All triboelectric measurements were performed at ambient laboratory temperature (22 °C) and relative humidity of (38 ± 1)%, without additional treatment [51] of the STG layer, so that the device performance reflects realistic indoor humidity conditions.

Triboelectric voltage signals were recorded using an oscilloscope (Infinivision 1000 X-series, 4ch, 100 MHz, DSOX1204A, Keysight, Santa Rosa, CA, USA) using a differential voltage probe to enable floating measurements and suppress ground-loop and capacitive coupling artifacts typical for high-impedance triboelectric systems. The short-circuit current was determined based on Ohm's law when a single discharge cycle passed through a known resistive load. The output power was evaluated over a broad range of load resistances from 1 kΩ to 500 MΩ, while the voltage was monitored by the oscilloscope connected in parallel to the load. Additionally, the generated charge was measured using an electroscope (GRD-BTA charge sensor) connected to a LabQuest

Table 2
Setting parameters used in TENG experiments.

Control voltage (V)	Pressure (kPa)	Velocity (m/s)
6	0.5	0.12
7	1.6	0.15
8	2.7	0.17
9	3.7	0.19
10	4.7	0.22
11	5.7	0.24
14	8.2	0.31
17	10.4	0.38
20	12.1	0.45
22	13.0	0.50
23	13.4	0.52
26	14.3	0.60
29	14.8	0.67

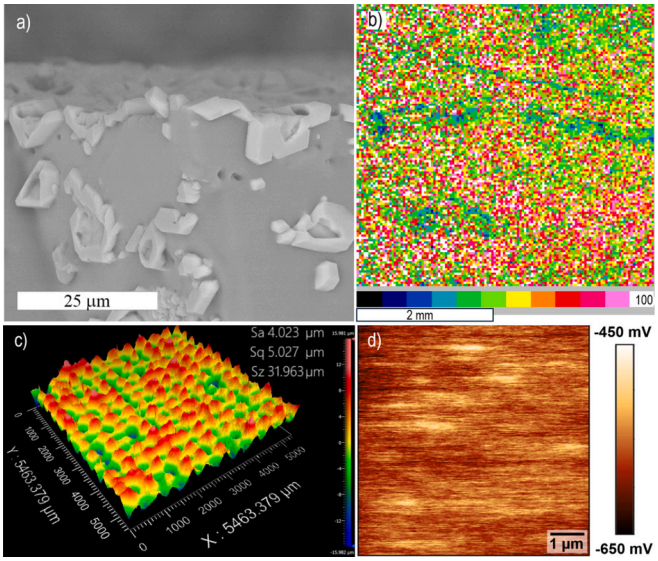

Fig. 3. Structural characterization of STG film: (a) SEM cross-section images of a fracture surface, (b) EDS sulfur distribution map, (c) 3D surface topography, and (d) KPFM surface potential map.

interface system (Vernier Edu-for s.r.o., Prague, Czech Republic).

The energy-harvesting capability of the STG was evaluated using a triboelectric nanogenerator operating in a vertical contact–separation mode, in which a mechanically actuated steel electrode periodically impacted the STG film. The generated AC triboelectric signal was rectified using a Graetz bridge composed of four Schottky diodes with an opening voltage of 1.5 V and subsequently stored in polymer-film capacitors with capacitances ranging from 10 to 128 nF (10, 22, 44, 66, 88, 108, and 128 nF). After charging, the stored energy was discharged through a resistive load corresponding to the 10 MΩ input impedance of the oscilloscope or used to power LEDs connected in series.

3. Results and discussion

3.1. STG characterization

Characterization of STG films is summarized in Figs. 3 and 4. SEM cross-sectional images of a fracture surface of the compression-molded STG film reveals a heterogeneous microstructure consisting of well-defined micron-sized domains of crystalline sulfur embedded in a continuous polymer matrix (Fig. 3a). An angular, faceted morphology of these domains is characteristic of crystalline sulfur and indicates phase separation during solidification. Sulfur-rich domains are distributed across the film cross-section, with locally increased occurrence near the surface. Elemental mapping by EDS illustrates the spatial distribution of sulfur at the STG surface with the signal normalized to sulfur (Fig. 3b). The corresponding elemental composition (C 43.5 wt%, O 31.2 wt%, S 25.4 wt%) indicates that sulfur is not overrepresented at the surface.

The 3D profilometry analysis of the STG film (Fig. 3c) shows highly regular surface morphology, characterized by a pattern of pyramid-like structures. This structured surface suggests that the STG is of a thermoplastic nature; the film replicates texture of a PTFE-coated glass fiber fabric release foil used during compression molding. The measured surface roughness parameters were Sa = 4.023 µm, Sq = 5.027 µm, and Sz = 31.963 µm. The surface profile of the stainless-steel counter-electrode was also analyzed by 3D profilometry revealing Sa = 0.136 µm, Sq = 0.178 µm, and Sz = 1.150 µm. It was mechanically polished to ensure

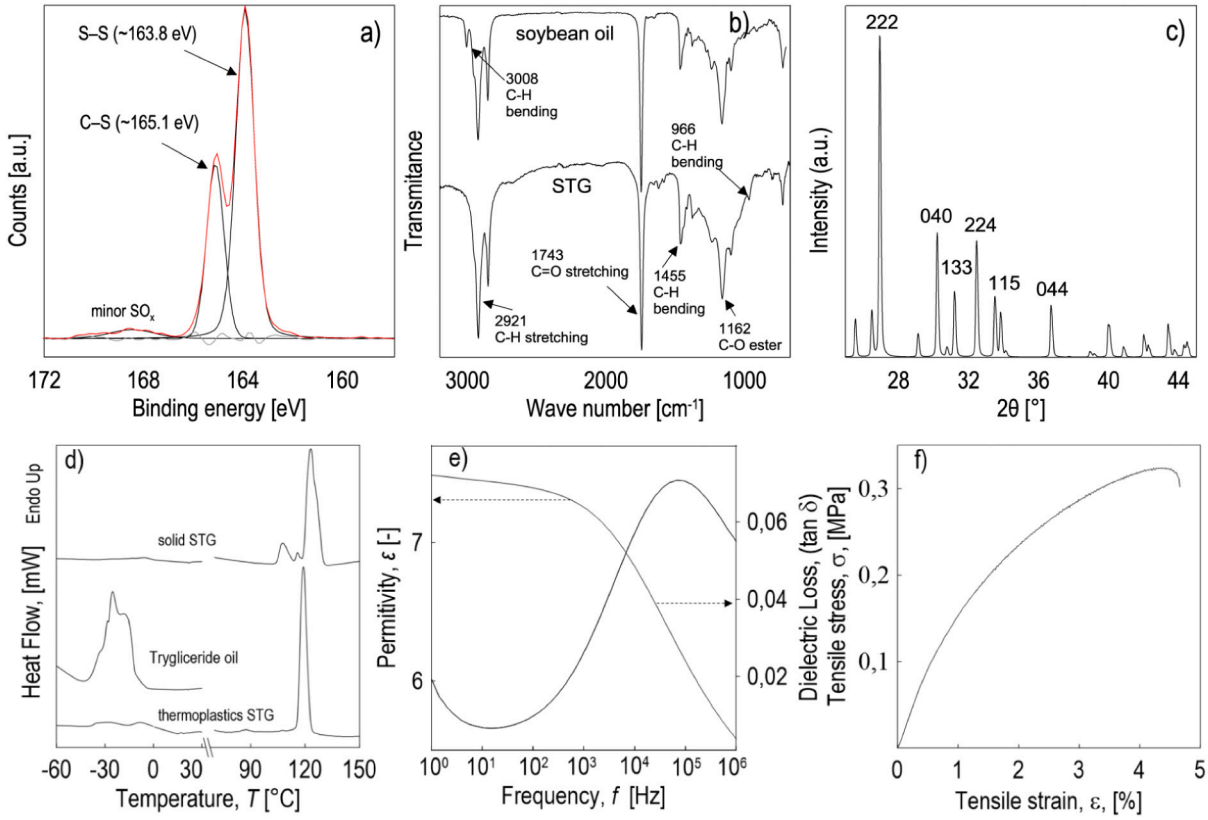

Fig. 4. Physicochemical characterization: (a) S 2p XPS spectrum of STG film, (b) FT-IR spectra of soybean oil and STG film, (c) XRD pattern of STG film, (d) DSC thermograms of soybean oil, STG polymer, and STG film (e) dielectric permittivity and loss tangent as a function of frequency of STG film, and (f) tensile stress–strain curve of STG film.

a smooth and uniform contact with the STG film.

AFM topography reveals a relatively smooth surface with a height variation below 120 nm over a 6 × 6 μm^2 scan area. The corresponding KPFM surface potential map (Fig. 3d) shows a laterally homogeneous contact potential difference ranging approximately from −650 to −450 mV, without pronounced localized potential domains or sharp potential gradients correlated with topographic features. The use of a smooth surface region minimizes electrostatic–topographic cross-talk, enabling reliable assessment of the surface potential distribution. The uniformly negative surface potential relative to the probe is consistent with an electron-rich surface state and agrees with the triboelectric behavior observed in contact–separation measurements.

X-ray photoelectron spectroscopy (XPS) analysis of the STG film (Fig. 4a) confirms the chemical incorporation of sulfur into the polymer network. The S 2p spectrum is dominated by a component at binding energies around 163.8 eV commonly assigned to S—S (disulfide/polysulfide) bonds. An additional contribution at approximately 165.1 eV is attributed to sulfur covalently bonded to carbon (C—S), indicating the formation of sulfur–carbon linkages within the STG matrix. A minor contribution corresponding to oxidized sulfur species (SO_x) is also observed, indicating a limited surface oxidation.

FT-IR spectra of the triglyceride oil precursor and the corresponding STG polymer are shown in Fig. 4b. The spectrum of soybean oil exhibits characteristic absorption bands of triglyceride esters, including aliphatic C—H stretching vibrations at ~2921 cm^{-1}, a strong ester carbonyl (C=O) stretching band at ~1743 cm^{-1}, C—H bending vibrations at ~1455 cm^{-1}, and C—O stretching of ester groups at ~1162 cm^{-1}. These characteristic bands are also present in the spectrum of the STG polymer, indicating that the triglyceride/ester backbone of the oil is preserved after inverse vulcanization. In contrast, the = C–H stretching band of unsaturated groups at ~3008 cm^{-1}, clearly observed in the oil precursor, disappears in the STG spectrum, while a new band appears at ~966 cm^{-1}. This spectral change indicates the consumption of carbon–carbon double bonds and chemical modification of the unsaturated segments during the inverse vulcanization process.

The X-ray diffraction (XRD) pattern of the STG film (Fig. 4c) exhibits several sharp diffraction peaks in the 2θ range between approximately 10° and 35°, which correspond to crystalline elemental sulfur. This assignment is confirmed by comparison with a reference sulfur diffraction pattern [52] and is consistent with previous studies of inverse-vulcanized sulfur–soybean oil polymers, where similar reflections were attributed to residual crystalline S_8 dispersed within an amorphous polymer matrix [53,54]. The presence of these reflections indicates that a fraction of sulfur remains unreacted in the crystalline form. No distinct diffraction peaks associated with the sulfur-crosslinked organic network are observed, suggesting that the polymeric STG phase is predominantly amorphous.

Further, the differential scanning calorimetry analysis was performed on the triglyceride oil precursor and STG film samples to evaluate thermal transitions and confirm the occurrence of the inverse vulcanization, Fig. 4d. The triglyceride oil exhibited an endothermic transition below 0 °C (onset at −25.86 °C), attributed to the melting of the crystalline fractions of the fatty acid chains. In contrast, this transition was absent in both the first and second heating scans of the STG film, indicating complete chemical incorporation of the oil into the sulfur-based network. In the first heating scan of the solid STG sample, three distinct endothermic peaks were observed between 119 and 124 °C (significant peak maxima at 120.8 °C and 123.9 °C), with a total melting enthalpy of −29 J/g. These peaks correspond to the melting of the unreacted crystalline sulfur [55]. The second scan of the compression-molded STG film showed a single melting peak at 119.4 °C with an enthalpy of −27.6 J/g, again confirming the absence of the phase transitions associated with the oil component.

The dielectric analysis of the STG film shows a frequency-dependent behavior of both the dielectric permittivity and the dielectric loss tangent over the range of 1 Hz to 1 MHz. The real part of the permittivity decreases from approximately 7.3 at 1 Hz to about 6.1 at 1 MHz, indicating moderate frequency dispersion typical of crosslinked polymer networks. This moderate relative permittivity supports sufficient electrostatic induction and charge storage at the triboelectric interface. The dielectric loss tangent exhibits a distinct relaxation peak centered around 100 kHz, which corresponds to slow polarization processes in the polysulfide network. The relatively low dielectric loss in the frequency range relevant for our cyclic mechanical actuation (typically 0.5–1 Hz) helps to suppress dissipative charge leakage and supports retention of the generated charges over time.

Based on the tensile test results of the STG film (Fig. 4), a tensile strength of 324 kPa, and an elongation at break of 4.4% were obtained. The tensile modulus of 0.16 GPa was calculated by a linear approximation in a strain range up to 1%. Importantly, these results confirm that the STG has sufficient intrinsic mechanical integrity to form self-supporting films, enabling practical application in layered triboelectric devices (see Supplementary Information Video V1) demonstrating mechanical flexibility of the resulting STG film.

3.2. Triboelectric response of STG-based TENG

XPS, FTIR, and DSC analyses confirm the formation of a crosslinked polysulfide network containing C—S and S—S bonds. Dielectric spectroscopy further reveals a combination of moderate relative permittivity and comparatively low dielectric loss in the frequency range relevant for our actuation conditions. The triboelectric behavior of the STG-based TENG was evaluated under cyclic loading using a solenoid-driven piston. Fig. 5a shows the open-circuit voltage response of the TENG during a single vertical contact and separation, in which the steel electrode (as illustrated in Fig. 2a) impacts the top surface of the STG film under a pressure pulse of 14.8 kPa corresponding to contact velocity of 0.67 m/s (Table 2) at frequency of 10 Hz. Following impact, the steel electrode remains in a macroscopic contact with the STG surface for approximately 50 ms before separating and rebounding, after which the next contact cycle occurs. The open-circuit voltage has a characteristic waveform starting with a sharp positive peak of an approximately 420 V. At the STG-steel interface, a charge separation occurs with the STG

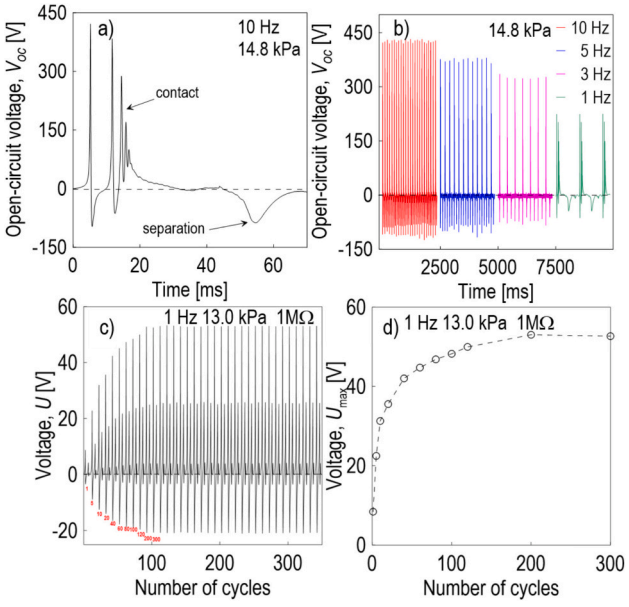

Fig. 5. Triboelectric response of STG/steel TENG to vertical contact-separation: a) open-circuit voltage profile during single impact (10 Hz, 14.8 kPa, 5 cm^2), b) frequency-dependent open-circuit voltage as function of time (14.8 kPa, 5 cm^2), c) representative output voltage during cyclic loading of more than 300 consecutive impacts and corresponding d) evolution of the maximum output voltage with number of cycles (1 MΩ, 1 Hz, 13 kPa, 5 cm^2).

surface becoming negatively charged and the steel positively charged. Redistribution of charges within the TENG structure through the external circuit gives rise to the observed voltage signal. Polarity of the recorded signal is defined by the connection of the oscilloscope anode to the Cu electrode. The observed polarity, indicated by the direction of the initial positive voltage peak, is consistent with tribonegative behavior of the STG surface upon contact with the tribo-positive steel electrode. Following the initial positive voltage peak, the signal transitions into a negative phase with an amplitude of approximately −110 V. This feature appears while the steel electrode remains in macroscopic contact with the STG surface, and is attributed to charge redistribution and relaxation processes at the polarized interface. Subsequently, a secondary positive voltage peak of approximately +350 V is observed, occurring during the same contact period.

This behavior is consistent with dynamically resolved contact–separation and relaxation processes, rather than with independent charging events. Using a combined experimental and modeling approach it has been shown [56,57], that the open-circuit voltage in contact–separation TENGs naturally decomposes into multiple peaks originating from electrostatic induction during approach, charge separation at impact, and subsequent evolution of the air gap and relaxation of the contacting surfaces.

Musa et al. [58] further resolved the charging events in contact–separation electrification and demonstrated that multi-peak *V*oc signals can be assigned to distinct stages of approach, contact, and separation, with their relative contributions depending on the tapping frequency. In analogy, we interpret the main peak in our *V*oc trace as dominated by electrostatic induction and initial charge separation at impact, while the secondary (and tertiary) peaks that occur without additional macroscopic separation are consistent with interfacial dielectric/mechanical relaxation of the STG/steel contact.

Fig. 5b compares the open-circuit voltage waveforms of the STG/steel TENG recorded at different frequencies (1, 3, 5 and 10 Hz) under the same nominal contact pressure of 14.8 kPa and in the same vertical contact–separation mode. With increasing excitation frequency, the individual voltage pulse shape remains essentially unchanged, while the pulse density in time increases; the peak open-circuit voltage reaches approximately 420 V at 10 Hz, decreases to about 380 V at 5 Hz, to approximately 320 V at 3 Hz, and further to about 230 V at 1 Hz. The slight increase in the peak open-circuit voltage with increasing excitation frequency is consistent with reduced charge relaxation between successive impacts, as shorter time intervals limit charge dissipation, while the impact force and velocity remain unchanged; the voltage waveform remains stable over the investigated frequency range. These frequency-dependent data show that the voltage waveforms remain qualitatively similar across the investigated frequency range.

The response shown in Fig. 5a corresponded to the stabilized state of the TENG after repeated cycling, while Fig. 5c shows the evolution of the voltage signal during 300 consecutive impact cycles under representative conditions (1 MΩ, 1 Hz, 13 kPa, 5 cm^2), recorded to assess the stabilization of the output under constant loading conditions. The output voltage gradually increases with each cycle during the initial phase, suggesting a progressive build-up of charge separation at the interface, related to the development of the interfacial polarization. Each cycle involves the impact of the steel electrode onto the STG surface, followed by 0.5 s contact hold, subsequent separation, and the next impact. To illustrate this development, the selected voltage responses corresponding to the specific cycles are shown with the respective cycle numbers (1, 5, 10, 20, 40, 60, 80, 100, 120, 200, and 300) marked in red under each curve. The voltage amplitude increases during the initial tens to hundreds of cycles and gradually approaches a quasi-steady state at higher cycle numbers. This behavior indicates a gradual stabilization of the interfacial charge state under repeated mechanical cycling.

Fig. 5d shows the evolution of the maximum output voltage (U_{max}) as a function of the number of cycles, extracted from the measurements shown in Fig. 5c. The maximum voltage increases progressively during the initial cycles, and gradually approaches a saturated value with increasing number of cycles. Under the applied conditions (1 MΩ load, 1 Hz excitation frequency, contact pressure of 13 kPa, and active area of 5 cm^2), U_{max} stabilizes at approximately 55 V. This behavior indicates a gradual stabilization of the interfacial charge state under repeated mechanical cycling, leading to a quasi-equilibrium voltage response during successive actuation cycles.

The sulfur-rich STG layer exhibits several characteristic features that support charge trapping and interfacial polarization effects. A progressive increase followed by stabilization of the output voltage during cyclic loading indicates the build-up of a semi-permanent interfacial polarization state. In addition, post-separation short-circuit experiments reveal a delayed voltage response whose magnitude scales with the prior contact time, consistent with gradual charge release from trapped or polarized interfacial states.

To evaluate the pressure sensitivity of the STG-based TENG in its quasi-steady state, the voltage outputs were recorded at different impact pressures (0.5 to 14.8 kPa), Fig. 6a. The curves represent stabilized signals measured after the initial phase described in Fig. 5c-d. The amplitude of the first positive peak increases with an applied pressure, indicating that the normal force at the impact plays a key role in increasing the triboelectric output under these conditions. Higher

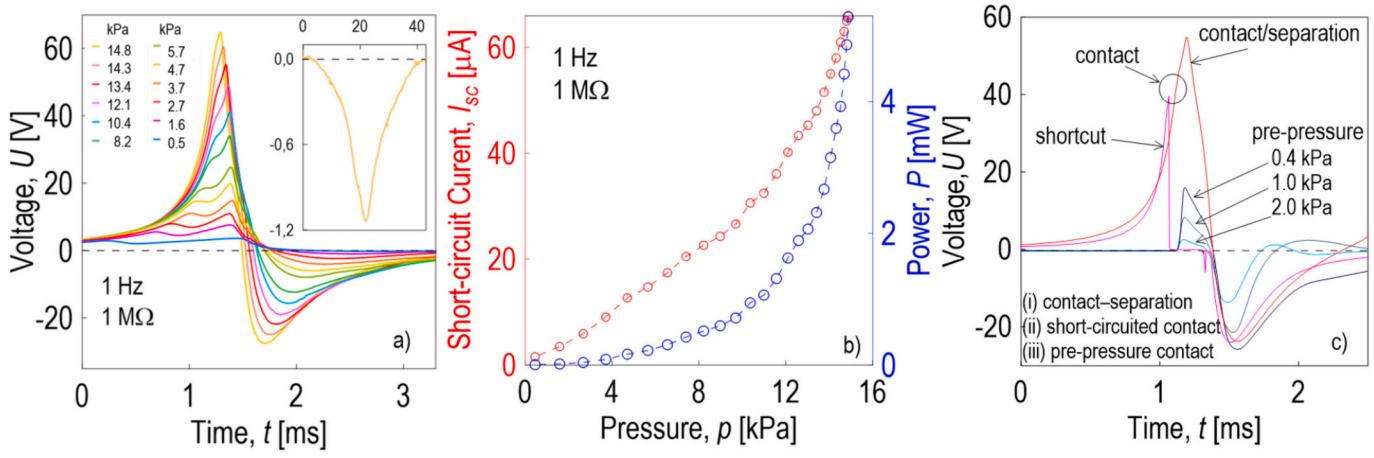

Fig. 6. Triboelectric response of STG/steel TENG to vertical contact-separation: a) output voltage profiles at various applied pressures, b) peak short-circuit current and power as a function of pressure (resistive load 1 MΩ, 1 Hz, 5 cm^2), c) comparison of three measurement modes illustrating mechanical origin of secondary and tertiary voltage features: conventional contact–separation, short-circuited contact configuration, and pre-pressure contact mode (0.4–2.0 kPa) (1 Hz, 14.8 kPa, 1 MΩ).

pressure improves the effective contact between the steel electrode and the STG surface, leading to an increased charge separation and a stronger electrostatic induction. Fig. 6b shows the dependence of the short-circuit current and output power on the applied pressure. Both quantities depend strongly on increasing pressure, reflecting enhanced electrical output under improved contact conditions.

A consistent feature observed under all tested loading conditions (Fig. 6a) is the presence of bimodal voltage peaks during the contact phase, which are particularly pronounced at lower impact pressures. Two distinct maxima are separated by a short delay. This feature becomes more pronounced at lower pressures, likely due to slower contact velocities, which may favor the temporal separation of multiple charge generation processes at the interface. The generation of voltage in TENG devices is not limited to the moment of a physical contact. When the opposing surfaces approach each other, an electrostatic induction occurs due to the imbalance of the charge generated, which causes the charge redistribution across the electrodes even before contact. According to the time analysis, the actual point of contact occurs near the first peak. The second voltage peak that follows shortly after has the same polarity, and consistently higher amplitude than the first one. This suggests that charge generation continues during or immediately after the physical contact, most likely due to the triboelectric charge separation. The two distinct maxima are interpreted as the result of temporally separated interfacial processes: the first corresponding to charge redistribution driven by electrostatic induction during surface approach and initial contact, and the second attributed primarily to triboelectric charge separation as the surfaces are brought together under applied pressure. For quantitative evaluation of the electrical output, a defined resistive load of 1 MΩ was used, and the voltage across this load was measured using a differential probe connected to the oscilloscope. Based on the peak voltage values obtained under these controlled load conditions, the corresponding peak current and instantaneous power were evaluated. Fig. 6b summarizes the resulting pressure dependence of the evaluated current and power, both of which increase monotonically with increasing applied pressure, providing a consistent comparison of device performance under identical resistive loading.

In addition, an experiment to directly probe the mechanical origin of the secondary and tertiary voltage features is shown in Fig. 6c. Three measurement modes are compared: conventional contact–separation operation, a short-circuited contact configuration, and a pre-pressure contact mode with restricted macroscopic motion of the steel electrode toward the STG layer.

In the conventional contact–separation mode (red curve), the voltage response exhibits a characteristic initial positive peak, with the moment of mechanical contact of the steel electrode with the STG surface indicated by the marked contact point. This primary peak shows a distinct change in slope, followed by a secondary positive maximum and a subsequent negative peak. After impact, no deliberate macroscopic separation is imposed and the steel electrode remains in contact with the STG surface over the measurement window, indicating that the observed post-contact features do not require macroscopic detachment but are associated with contact-related interfacial processes.

A negative peak was also observed on the magenta curve, measured in the same dynamic mode, but with a thin silver coating deposited on the bottom copper electrode. This conductive layer created a short-term short-circuit condition at the moment of the contact, which caused the signal to drop to zero. The subsequent negative voltage peak observed after release of the short-circuit condition is therefore attributed to local interfacial relaxation and evolution of the effective contact area, or a transient micro-rebound, rather than to macroscopic separation of the contacting surfaces.

In the pre-pressure contact mode (blue curves), the steel electrode is pressed against the STG surface prior to excitation by a defined static preload, such that macroscopic approach and separation are strongly restricted. As a result, the initial voltage rise associated with electrostatic induction during surface approach is absent, and the voltage response originates predominantly from contact-related processes. Following the main positive maximum, the signal evolves into a negative peak, consistent with interfacial polarization dynamics and dielectric/mechanical relaxation occurring within the contacting interface rather than with gap-dependent induction effects.

The resistive load-dependent electrical performance of the STG/steel contact–separation TENG measured at an applied pressure of 14.8 kPa for two excitation frequencies (1 and 10 Hz) is shown in Fig. 7. The device exhibits a well-defined maximum power point (MPP) at an external load resistance of approximately 1 MΩ for both excitation

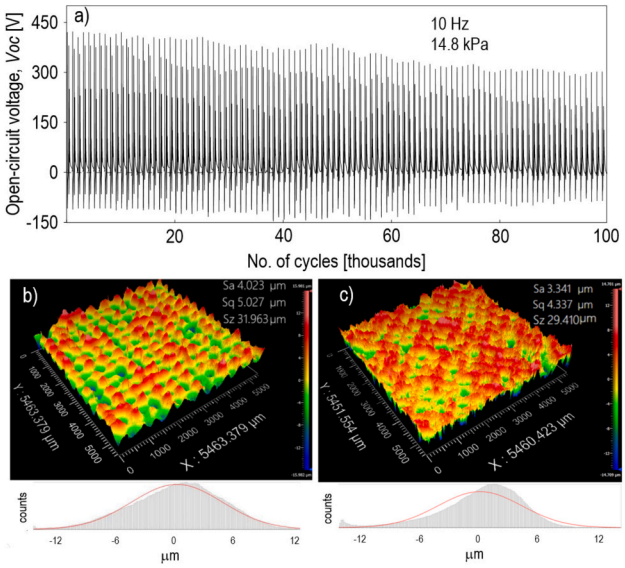

Fig. 8. Long-term durability of STG-based TENG (vertical contact-separation, 10 Hz, 14.8 kPa, 5 cm^2): (a) evolution of open-circuit voltage recorded over 10^5 mechanical cycles (each 1000th cycle shown for clarity), and 3D optical profilometry of pristine surface (b) and STG surface after 100,000 contact–separation cycles (c).

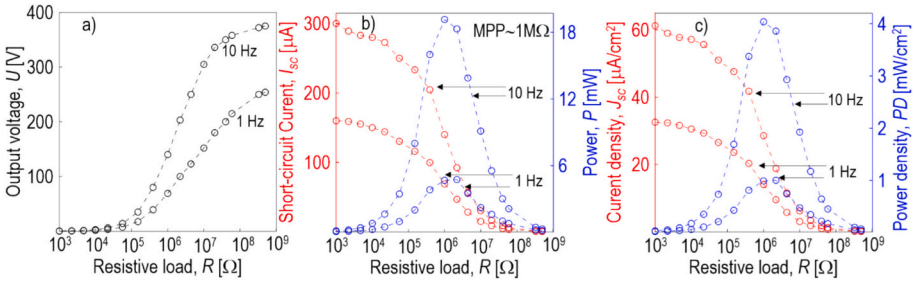

Fig. 7. Resistive load dependent a) output voltage, b) short-circuit current and power, and c) current density and power density of STG/steel TENG (vertical contact-separation, 1 and 10 Hz, 14.8 kPa, 5 cm^2).

frequencies. This behavior suggests that the effective internal impedance of the TENG is on the order of 10^6 Ω and that matching the external load to this value is essential to achieve the maximum electrical power output and power density from the STG layer. At the maximum power point near 1 MΩ, the STG-based TENG delivers a maximum output power density of approximately 4.05 mWcm^{-2} under an applied pressure of 14.8 kPa. Under low-resistance loading conditions (10 kΩ), peak output currents of up to ~60 μAcm^{-2} are obtained, illustrating the current delivery capability of the device.

3.3. Durability, stability and benchmarking to sulfur-based TENGs

A long-term durability of the STG-based TENG was evaluated under repeated vertical contact–separation cycling. Fig. 8a shows the evolution of the open-circuit voltage *V*oc recorded over 10^5 mechanical cycles at an excitation frequency of 10 Hz and an applied pressure of 14.8 kPa. Throughout the entire cycling test, the characteristic voltage waveform is preserved without signal collapse or irregular behavior. The maximum amplitude of the first positive voltage peak gradually decreases from approximately 420 V at the beginning of the test to about 300 V after 10^5 cycles, while the overall waveform shape remains unchanged, indicating stable electrical operation under prolonged loading.

The durability of STG film surface can be also observed from 3D surface scanning. For both, the pristine surface (Fig. 8b) and the surface after 10^5 cycles (Fig. 8c), the height distributions exhibit an approximately Gaussian shape, indicating a statistically homogeneous surface morphology without the formation of localized defects. After 10^5 contact–separation cycles, the distribution shows a slight shift toward higher relative height values, accompanied by a reduction of extreme positive height excursions. This behavior is consistent with mild smoothing of the highest surface asperities under repeated mechanical loading, rather than with structural damage or material removal.

The sulfur-based TENG literature provides three high-performance reference systems against which the sulfur–triglyceride (STG) results might be benchmarked (Table 3): a sulfur-rich polymer synthesized via inverse vulcanization of elemental sulfur with an organic comonomer (SRP)/two-dimensional transition-metal carbides and nitrides (MXene) composite device, a fluorinated sulfur copolymer blend based on poly (sulfur-random-1,3-diisopropenylbenzene) (poly(S-r-DIB)) with poly (2,3,4,5,6-pentafluorostyrene) (PPFS), and a directly fluorinated (F_2) poly(S-r-DIB) sulfur copolymer.

In the SRP/MXene system reported by Cho et al. [31], a sulfur-rich inverse-vulcanized polymer matrix is filled with a low content of MXene nanosheets forming a segregated structure. Choi et al. [30] used poly(S-r-DIB) and enhance its tribo-negative character by physically blending 7.5 wt% PPFS; during hot pressing, the highly fluorinated PPFS migrates to the surface and forms a fluorinated interface, which is treated with corona. In an earlier approach, Lee et al. [29] directly fluorinated a poly(S-r-DIB) film using molecular fluorine gas, producing a thin fluorinated surface layer. Across these three systems, high output relies on combining sulfur-rich backbones (SRPs such as poly(S-r-DIB)) with either PPFS or direct F_2 treatment, or MXene filler, and in the most powerful demonstrations also with corona poling to maximize and stabilize surface charge density.

In contrast, the STG material in this work is a sulfur–triglyceride polymer synthesized by solvent-free inverse vulcanization of elemental sulfur with waste vegetable oil, processed into ~0.5 mm compression-molded films without fluorination (PPFS or F_2) or corona treatment. The STG TENG operates in a vertical contact–separation configuration with a stainless-steel electrode driven by a solenoid actuator, and under cyclic loading it exhibits progressive charge accumulation, stabilizing at a maximum output voltage of 420 V, a short-circuit current of 60 μAcm^{-2}, a triboelectric charge density of −32.8 μCm^{-2}, and a power density of 4.05 mWcm^{-2} at an external load of 1 MΩ. Although these absolute electrical outputs are lower than those of the corona-poled SRP/MXene composite or the fluorinated poly(S-r-DIB) and PPFS-modified systems, the STG device offers a distinct environmental and materials advantage: it is derived entirely from low-value waste streams (desulfurization sulfur and used frying oil), avoids fluorinated additives such as PPFS and hazardous F_2 gas, and therefore circumvents concerns related to persistent fluorinated pollutants, while still enabling efficient triboelectric polarization and exhibiting a unique mechanically induced interfacial polarization with delayed electrical response that has not been reported yet.

Table 3
Benchmarking of sulfur based TENGS in vertical contact-separation mode comparing open-circuit voltage *V*oc, peak output voltage *V*, short circuit current *I*sc, peak short-circuit current *I*, current density *J*, power *P*, power density *PD*, operating force *F*, frequency *f*, and device area *A*.

TENG	*Voc*	*V*	*Isc*	*I*	*J*	*P*	*PD*	*F*	*f*	*A*
	V	V	μA	μA	μA/cm²	mW	mW/cm²	N	Hz	cm²
STG	420	-	300	-	60	19	4.05	7.4	10	5
SRP/MXene [31]	-	331	-	20	-	1.01	0.081*	30	0.65	12.5
SRP/MXene – corona [31]	-	1718	-	129	-	-	0.38*	30	0.65	81
poly(S-r-DIB)/PPFS [30]	164	-	-	2.1	-	0.14	0.012**	30	0.65	12.5
poly(S-r-DIB)/PPFS – corona [30]	1362	-	25.3	-	-	3.67	0.045**	30	0.65	81
F_2/poly(S-r-DIB) – corona [29]	1366	-	18	-	-	-	-	30	1.3	81

Note: steel electrode for STG, others Al; *at 8 MΩ, **at 100 MΩ.

3.4. Mechanically induced interfacial polarization and delayed electric response

To evaluate the contribution of the interfacial polarization to the electrical output of the STG-based TENG outside dynamic cycling, the post-separation short-circuit measurement were performed, Fig. 9. In the first stage (a), the steel electrode approaches the STG surface while the external circuit is connected. The observed voltage comes from the residual interfacial polarization induced by previous triboelectric interactions, and is attributed to the electrostatic induction ($U > 0$ V). In the second phase (b), the physical contact between the steel electrode and the STG surface results in the triboelectric charge separation, which drives additional electron flow through the external circuit and produces the voltage signal with the same polarity as in the first phase ($U > 0$ V), thus enhancing the previously total output. The layers are then held in the stationary contact for the defined period of time during which no mechanical motion occurs. In the third phase (c), after the contact period, the layers are mechanically separated, while the external circuit remains open. This separation induces the charge imbalance through the triboelectric charge separation and electrostatic induction, which cannot be compensated externally, and therefore remains confined within the system. In the final phase (d), the circuit is closed after the mechanical separation (short-circuit measurement after separation), allowing the uncompensated interfacial charge to drive the electron flow between the electrodes, resulting in the negative output voltage ($U < 0$ V). This measurement scheme allows to investigate the delayed electrical response arising from the triboelectrically prepolarized interface.

Voltage decay curves (Fig. 9 right) are recorded during post-contact and post-separation measurements. The red curves represent exponential fits to the experimental data confirming the capacitor-like discharge behavior in both cases. The lower curve corresponds to the post-separation measurement described in the scheme (a–d), where the pre-polarized interface is separated under open circuit conditions and the circuit is closed only after separation. The sharp negative voltage (-72 ± 3 V) is observed upon switching, which gradually decreases over time. This delayed response arises from the release of the interfacial charge imbalance that was created during the mechanical separation, and clearly indicates that the polarization was stored in the system before the electric activation. The upper curve, on the other hand, is the results from a post-contact measurement, which is not shown in the scheme in Fig. 9. Here, the electrical contact occurs only after the electrodes are brought together under open circuit conditions. When the circuit is closed, the positive output voltage (66 ± 3 V) is observed,

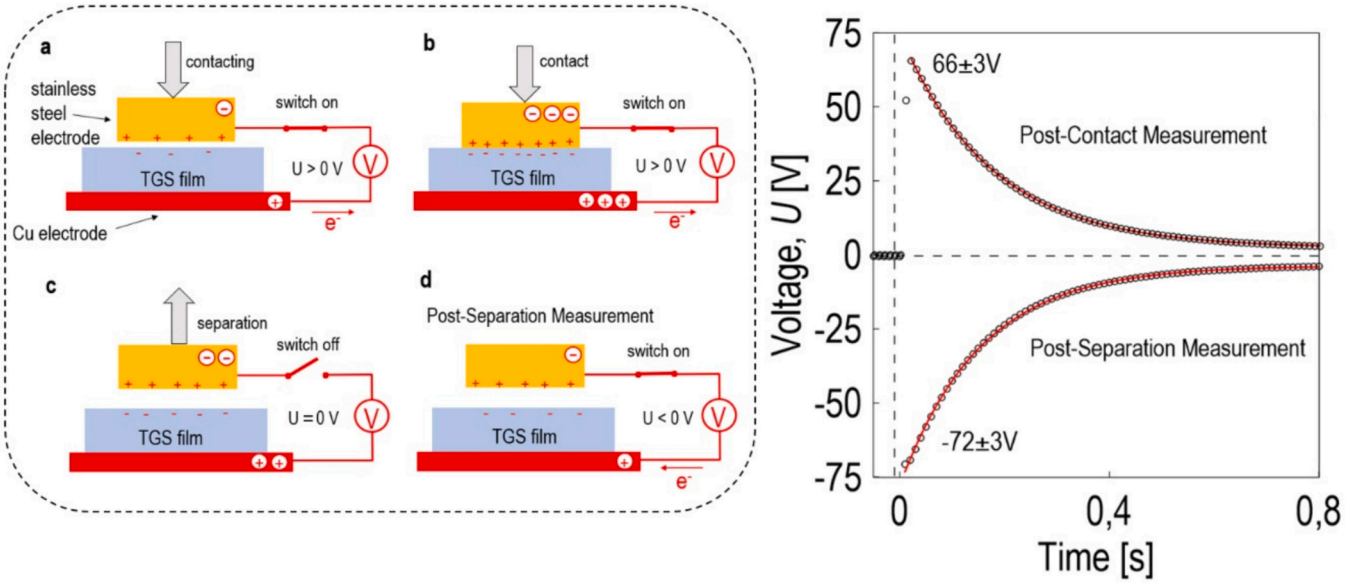

Fig. 9. Scheme of post-separation short-circuit measurement used to evaluate delayed electrical response of a triboelectrically prepolarized STG interface, and voltage decay curves recorded for post separation and post contact measurements.

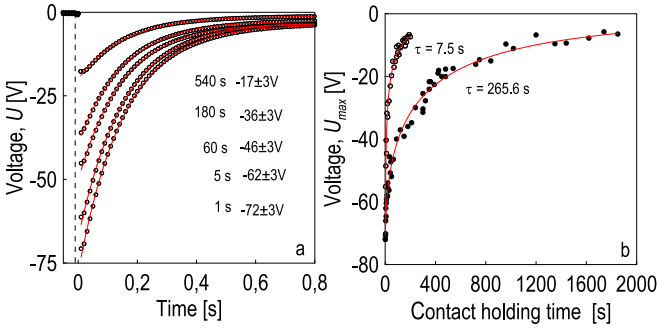

Fig. 10. Post-separation voltage (U) response curves recorded after various contact holding times, and maximum output voltage U_{max} as a function of contact holding time fitted with exponential functions (1 Hz, 14.8 kPa, 1 MΩ).

which again exhibits a capacitor-like decay profile. It is noteworthy that even after the delay of 30 s after the contact, the system retains +30 V, and after 10 min, the residual voltage of +5 V can still be measured.

Fig. 10 shows the evolution of the delayed voltage output during the post-separation measurements as a function of contact holding time. Although the interfacial polarization likely decreases during the prolonged contact, the delayed voltage response observed upon the separation confirms that the residual polarization remains, and continues to affect the magnitude of the generated output. The observation of a signal of 17 ± 3 V after 540 s of the contact indicates that the duration of the contact has a significant effect on the state of the interface, which in turn affects the magnitude of the voltage generated upon separation. This effect is summarized by plotting the maximum voltages U_{max} as a function of the contact holding times.

The data follow an exponential decay giving a time constant τ of 265.6 s, which characterizes the temporal evolution of the interfacial state under the static contact conditions. In comparison, an alternative post-separation measurement, where the system remained in the separated state during the holding phase before reconnection, yielded much shorter time constant of approximately 7.5 s. This difference suggests that maintaining physical contact between the TENG layers plays an important role in stabilizing the interface and slowing down its relaxation.

This type of the delayed charge release, generated by purely mechanical means and manifesting only upon subsequent electrical switching, supports the interpretation of the system as a mechanically polarized capacitor. The τ values define a characteristic timescale of interfacial polarization retention rather than a parameter governing continuous harvesting performance. Such behavior is relevant for event-driven or delay-based functionalities, such as mechanically written and electrically read states, self-powered delay or trigger elements, and mechanical history indicators, rather than for maximizing continuous energy harvesting.

3.5. Triboelectric material pairing and area scaling

Fig. 11 summarizes the triboelectric charge density (TECD) of representative polymeric and waste-derived materials referenced to stainless steel as a counter-electrode, obtained under identical experimental conditions (14.8 kPa, 1 Hz, 5 cm^2). The representation positions STG within the triboelectric series and enables rational selection of suitable tribopositive counterparts. The relatively strong negative TECD of STG confirms its suitability as a tribonegative layer derived from waste-based sulfur–triglyceride.

In the context of wearable electronics, three materials – PVAc, leather and commercially available nylon stockings were selected as

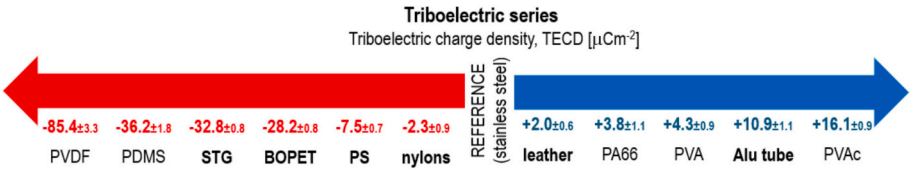

Fig. 11. Triboelectric charge density (TECD) series of representative polymeric and waste-derived materials referenced to stainless steel as a counter-electrode.

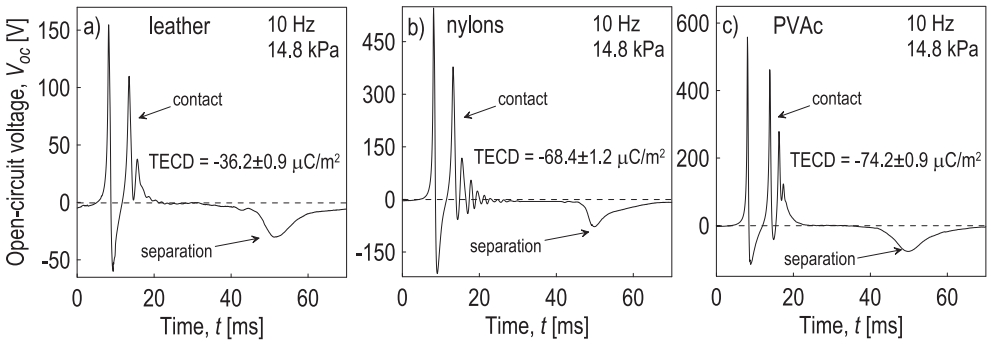

Fig. 12. Open-circuit voltage of STG-based TENGs paired with wearable-relevant counter materials: (a) leather, (b) nylon stockings, and (c) PVAc (vertical contact–separation, 10 Hz, 14.8 kPa, 5 cm^2).

application-relevant triboelectric partners. These materials represent practically important classes of substrates: commercial nylons and natural leather are materials already widely explored for flexible and skin-conformal TENGs, while PVAc is a low-cost adhesive that can be coated onto fabrics to impart a positive triboelectric layer. Leather and PVAc exhibit positive TECD values, ensuring a large charge-density contrast when paired with strongly negative STG, while nylon stockings are included primarily because they reflect realistic consumer-grade surfaces for wearable devices rather than for the intrinsic tribo-positivity of PA66.

The time-resolved *Voc* traces for STG paired with leather, nylon stockings and PVAc at 10 Hz and 14.8 kPa (Fig. 12) directly confirm that the electrical response scales with the TECD difference relative to STG rather than with the absolute position in the stainless-steel-referenced series. For the STG/leather pair, which exhibits the smallest TECD contrast (-36.2 ± 0.9 μC/m^2 relative to STG), the device produces the lowest *Voc* peak. In contrast, STG/nylon stockings show a substantially larger TECD contrast (-68.4 ± 1.2 μC/m^2), accompanied by markedly higher *Voc* peaks reaching approximately 530 V and a more pronounced separation-induced voltage waveform, indicating enhanced charge transfer per cycle. As expected, the STG/PVAc pair yields the highest *Voc* amplitude, approaching 570 V under the same operating conditions. Although the *Voc* amplitude scales with the TECD difference between the paired materials, the overall electrical performance is also influenced by real contact mechanics, surface topography, mechanical compliance, dielectric properties, and interfacial charge trapping and relaxation.

In the following, PVAc was selected as the tribopositive counterpart for detailed electrical characterization of STG. Fig. 13 summarizes the resistive-load-dependent electrical performance of the STG/PVAc contact–separation TENG. With increasing external load resistance (Fig. 13a), the output voltage increases while the current decreases; the output power reaches a maximum value of approximately 23 mW at an optimal load resistance of ~2.2 MΩ, corresponding to a power density of ~4.9 mW cm^{-2} for the active device area of 5 cm^2. Across the investigated frequency range (0.01–10 Hz), the position of the maximum power point remains essentially unchanged at a load resistance of approximately ~2.2 MΩ, Fig. 13b.

At excitation frequencies of 1 Hz and above, the power density and its maximum does not vary with frequency (Fig. 13b), suggesting that the interfacial polarization generated during contact is effectively preserved over successive cycles on the relevant time scale of mechanical actuation. At very low excitation frequencies (≤ 0.1 Hz), a systematic reduction in the maximum power density is observed. This behavior indicates partial relaxation of the interfacial polarization during the extended separation time between consecutive contact events, resulting in a gradual decay of the interfacial polarization of the TENG interface, and consequently lower triboelectric charge separation and electrostatic induction in the subsequent cycle.

The long-term stability of the open-circuit voltage output of the STG/PVAc TENG under repeated mechanical excitation of 10,000 contact–separation cycles (Fig. 13c) shows the stable *Voc* signal with identical amplitude and waveform shape throughout the test.

The effect of the active device area on the electrical output characteristics of the STG/PVAc contact–separation TENG is depicted in Fig. 14. To ensure controlled mechanical excitation during the scaling experiments, all measurements were performed under a constant applied pressure 3.7 kPa. The peak *Voc* increases systematically with increasing device area, reaching approximately 256 V for 4 cm^2, 389 V for 9 cm^2, and up to 704 V for 24 cm^2, while the overall waveform shape remains similar, Fig. 14a. The resistive load–voltage characteristics (Fig. 14b) indicate that, when normalized to the active area, smaller devices exhibit higher voltage output per unit area, suggesting more efficient charge utilization compared to larger-area configurations. In

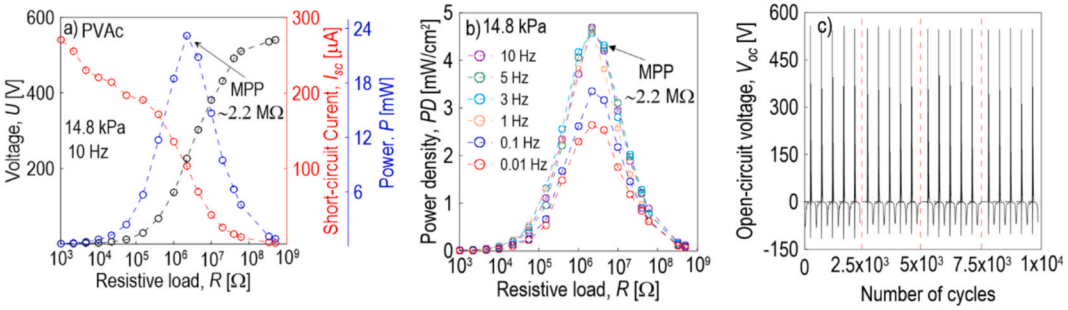

Fig. 13. Characteristics of STG/PVAc contact–separation TENG: (a) resistive load-dependent voltage, short-circuit current and output power (10 Hz, 14.8 kPa, 5 cm^2), (b) power density vs. resistive load as a function of frequency (14.8 kPa, 5 cm^2), and (c) open-circuit voltage output recorded for 1,000,010,000 cycles (10 Hz, 14.8 kPa, 5 cm^2).

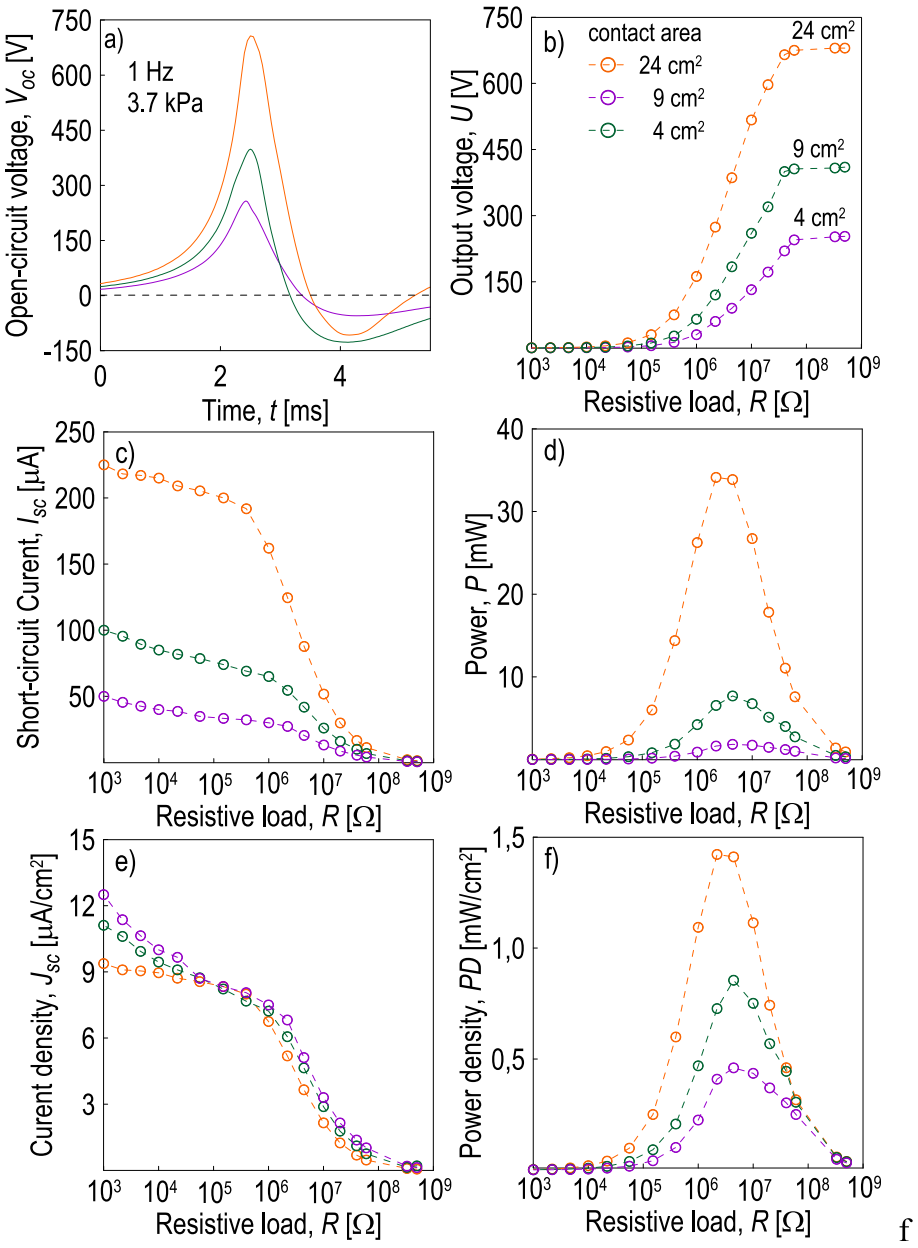

Fig. 14. Characteristics of STG/PVAc TENG evaluated at various active device areas: (a) time-dependent open-circuit voltage, and resistive load-dependent voltage (b), short-circuit current (c), power (d), current density (e), and power density (f) in vertical contact separation (10 Hz, 3.7 kPa).

absolute terms (Fig. 14b,c), both output current (μA) and power (mW) increase systematically with increasing active area, demonstrating that larger devices enable higher total electrical output. The corresponding load-dependent output current increases with active area, consistent with larger effective charge transfer (Fig. 14c). For example, at a load resistance of 10 kΩ, the device with an active area of 24 cm^2 delivers approximately 225 μA, while smaller-area devices generate proportionally lower absolute currents. Fig. 14d presents the load-dependent output power for different active areas, showing a well-defined maximum at an optimal load resistance of approximately 2.2 MΩ for all investigated device sizes. The maximum output power reaches ~35 mW for the largest device. When normalized to the active area, comparable current densities are obtained for different device sizes over most of the resistance range (Fig. 14e), except in the very low load-resistance region. Below approximately 22 kΩ, the area-normalized current density becomes higher for smaller active areas, indicating more effective charge transfer per unit area in the low-resistance regime. The corresponding power density as a function of load resistance is depicted in Fig. 14f with the maximum of approximately 1.45 $mWcm^{-2}$ for the 24 cm^2 device under an applied pressure of 3.7 kPa.

These results demonstrate that the electrical output of the STG/PVAc TENG can be effectively increased by enlarging the active device area. While the absolute voltage, current, and output power scale positively with device size, the area-normalized current and power density show sub-linear scaling. This behavior is likely related to non-uniform pressure distribution, incomplete real contact, and mechanical constraints that become more pronounced over larger active areas [59–61].

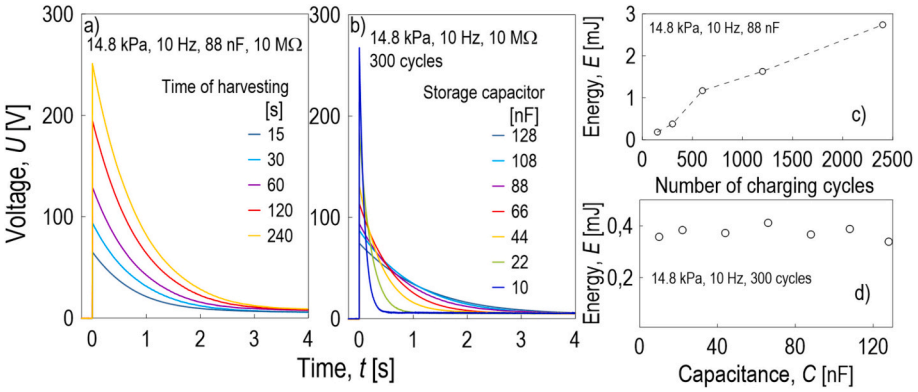

Fig. 15. Energy harvesting and storage characteristics of STG/steel TENG: (a) voltage decay after different energy harvesting times, (b) voltage decay for different storage capacitances after 300 charging cycles, (c) stored energy as a function of charging cycles, and (d) stored energy as a function of storage capacitance (vertical contact-separation, 14.8 kPa, 10 Hz, 5 cm^2).

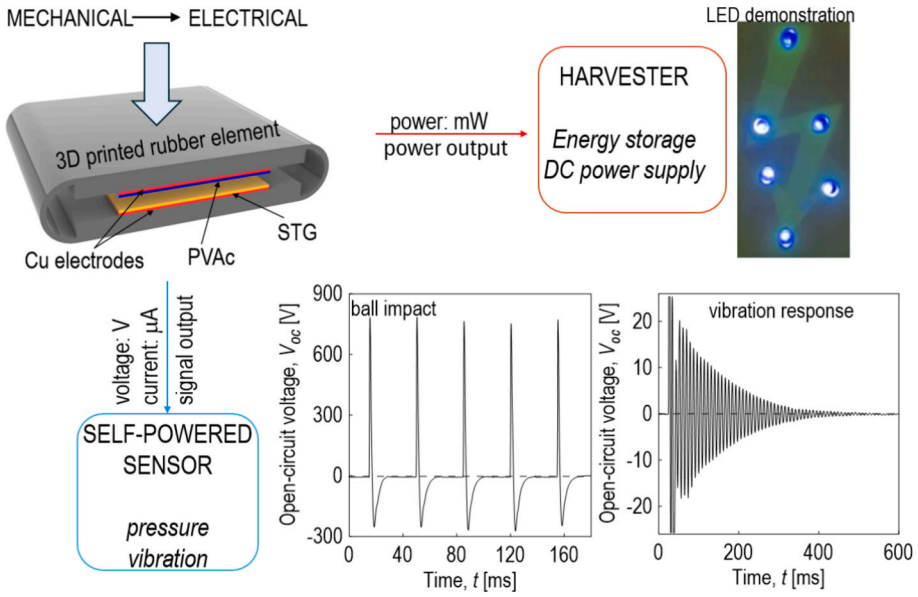

Fig. 16. Demonstration of energy harvesting and self-powered sensing using the STG/PVAc contact–separation TENG (contact area 24 cm^2).

3.6. *Energy harvesting using STG-based TENG*

The energy harvesting capability of the STG paired with steel electrode was evaluated using a TENG operating in a vertical contact–separation mode (described in 2.2). Discharge voltage $U(t)$ measured on a storage capacitor with a capacitance of 88 nF after different harvesting times (15, 30, 60, 120, and 240 s) under identical mechanical conditions (14.8 kPa, 10 Hz) is shown in Fig. 15a. The recorded curves represent the voltage decay during discharge of the capacitor through a resistive load of 10 MΩ after it had been charged by the rectified output of the TENG. Increasing harvesting time results in a systematic increase of the initial discharge voltage, exceeding 250 V after 240 s, while the overall decay profile remains unchanged. This behavior indicates progressive charge accumulation under continued mechanical excitation rather than a modification of the discharge mechanism. Fig. 15b shows the discharge voltage $U(t)$ measured through a constant resistive load of 10 MΩ for different storage capacitances (10–128 nF) after a fixed harvesting duration of 300 mechanical cycles under identical mechanical conditions.

Figs. 15c-d provide a quantitative interpretation of the energy harvesting process derived from the discharge measurements. Stored electric energy ($E = ½CU_0^2$) increases monotonically with a number of charging cycles (for a fixed capacitance of 88 nF), indicating that successive contact–separation events contribute reproducibly to the harvested energy. The observed behavior confirms that the amount of harvested energy is governed by cumulative mechanical excitation, demonstrating effective energy accumulation during repeated operation of the STG/steel TENG. Fig. 15d shows that for a fixed harvesting duration of 300 mechanical cycles, the total stored energy remains nearly constant over a wide range of storage capacitances (10–128 nF), despite the strong dependence of the peak discharge voltage on a capacitance observed in Fig. 15b. This indicates that the harvested energy is primarily determined by the mechanical excitation conditions and the number of charging cycles, while the storage capacitance mainly affects voltage level and discharge time profile.

STG/PVAc contact–separation TENG was further evaluated for practical self-powered sensing applications; a proof-of-concept demonstration illustrating the conversion of mechanical stimuli into usable electrical signals and harvested energy is shown in Fig. 16. The STG/PVAc TENG integrated with copper electrodes and a compliant 3D-

printed rubber support, enabling mechanical-to-electrical energy conversion under external loading, generated electric output, which can be directly used either as a sensing signal or routed through an external harvesting circuit for energy storage and DC power supply. The representative open-circuit voltage responses under two types of mechanical excitations: impulsive mechanical loading (ball impact) produces sharp, high-amplitude voltage peaks, while continuous vibrational excitation generates a damped oscillatory voltage response characteristic of the applied mechanical input. These results demonstrate the capability of the STG/PVAc TENG to function both as an energy harvester and as a self-powered sensor for pressure and vibration stimuli.

4. Conclusions

In this study, we demonstrated that triglyceride–sulfur (STG) polymer synthesized by an inverse vulcanization from waste-derived materials exhibits promising properties as sustainable, tribo-negative and mechanically robust material for contact–separation triboelectric nanogenerators (TENGs), showing stabilized output under repeated cycling. The STG film is readily processable as a thermoplastic and enables repeatable device fabrication and scaling across multiple active areas. A performance summary links electrical output to mechanical excitation parameters as follows:

- Electrical output vs. pressure: Increasing applied pressure (0.5–14.8 kPa) leads to higher open-circuit voltage, short-circuit current, and delivered power, indicating enhanced charge transfer per cycle due to improved interfacial contact.
- Electrical response vs. frequency: Frequency-dependent tests (1–10 Hz) show similar voltage waveform shapes across the investigated range, with a moderate increase in peak *V*oc at higher frequencies, consistent with reduced relaxation between successive impacts.
- The STG-based devices reach maximum power densities of ~4.05 $mWcm^{-2}$ for STG/steel (≈1 MΩ, 14.8 kPa, 10 Hz) and ~ 4.9 $mWcm^{-2}$ for STG/PVAc (≈2.2 MΩ, 14.8 kPa, 10 Hz), demonstrating competitive performance within the class of waste-derived triboelectric materials.
- Long-term cycling confirms stable output up to 10^5 cycles, indicating durable mechanical integrity.

Post-separation short circuit measurements provided clear evidence of delayed voltage generation, indicating that the interfacial polarization can be mechanically induced and maintained for extended periods of time. The dependence of the output voltage on the duration of contact prior to separation suggests that the interface retains the memory of the previous mechanical interaction. This type of the delayed charge release, generated purely through mechanical means and only manifested upon subsequent electrical switching, opens the possibility of interpreting the system as a mechanically polarized capacitor.

Based on normalized performance and benchmarking, the main novelty of the STG TENG is the combined (1) a simple, scalable processing route (thermoplastic film formation from inverse vulcanization) that delivers long-term operational stability up to 10^5 cycles, (2) demonstrating that a fully waste-derived inverse-vulcanized polymer can deliver competitive power output while maintaining material sustainability, (3) observed delayed-charge release upon electrical switching represents an additional relaxation-driven response of the STG TENG, distinct from its conventional energy-harvesting and self-powered sensing functions.

CRediT authorship contribution statement

Petr Slobodian: Writing – original draft, Visualization, Validation, Resources, Methodology, Investigation, Data curation, Conceptualization. **Berenika Hausnerova:** Writing – review & editing, Visualization, Resources, Conceptualization. **Cesar Alfredo Barbero:** Methodology, Investigation. **Pavel Riha:** Writing – review & editing.

Ethical compliance

Any procedure performed in this study does not involve human participants.

Funding

This work was supported by the Ministry of Education, Youth, and Sports of the Czech Republic within the framework of DKRVO (RP/CPS/2024-2028/005).

Declaration of competing interest

The authors declare that they have no known competing financial interests or personal relationships that could have appeared to influence the work reported in this paper.

Appendix A. Supplementary data

Supplementary data to this article can be found online at https://doi.org/10.1016/j.cej.2026.174416.

Data availability

Data will be made available on request.

References

[1] J.M. Chalker, M.J. Worthington, N.A. Lundquist, L.J. Esdaile, Synthesis and applications of polymers made by inverse vulcanization, Sulfur Chem. 377 (2019) 125–151, https://doi.org/10.1007/s41061-019-0242-7.
[2] M.J. Worthington, R.L. Kucera, J.M. Chalker, Green chemistry and polymers made from sulfur, in: Green Chem. 19, 2017, pp. 2748–2761, https://doi.org/10.1039/C7GC00014F.
[3] A.D. Smith, C.D. McMillen, R.C. Smith, A.G. Tennyson, Copolymers by inverse vulcanization of sulfur with pure or technical-grade unsaturated fatty acids, J. Polym. Sci. 58 (2020) 438–445, https://doi.org/10.1002/pol.20190138.
[4] M.J. Worthington, C.J. Shearer, L.J. Esdaile, J.A. Campbell, C.T. Gibson, S.K. Legg, Y. Yin, N. Lundquist, J.R. Gascooke, I.S. Albuquerque, J.G. Shapter, G. G. Andersson, D.A. Lewis, G.J.L. Bernardes, J.M. Chalker, Sustainable polysulfides for oil spill remediation: repurposing industrial waste for environmental benefit, Adv. Sustainable Syst. 2 (2018) 1800024, https://doi.org/10.1002/adsu.201800024.
[5] C.V. Lopez, A.D. Smith, R.C. Smith, Evaluation of animal fats and vegetable oils as comonomers in polymer composite synthesis: effects of plant/animal sources and comonomer composition on composite properties, Macromol. Chem. Phys. 224 (2023) 2300233, https://doi.org/10.1002/macp.202300233.
[6] M. Mann, J.E. Kruger, F. Andari, J. McErlean, J.R. Gascooke, J.A. Smith, M.J. H. Worthington, C.C.C. McKinley, J.A. Campbell, D.A. Lewis, T. Hasell, M. V. Perkins, J.M. Chalker, Sulfur polymer composites as controlled-release fertilisers, Org. Biomol. Chem. 17 (7) (2019) 1929–1936, https://doi.org/10.1039/C8OB02130A.
[7] I. Bu Najmah, N.A. Lundquist, M.K. Stanfield, F. Stojcevski, J.A. Campbell, L. J. Esdaile, C.T. Gibson, D.A. Lewis, L.C. Henderson, T. Hasell, J.M. Chalker, Insulating composites made from sulfur, canola oil, and wool, ChemSusChem 14 (2021) 2352–2359, https://doi.org/10.1002/cssc.202100187.
[8] A. Nayeem, M.F. Ali, J.H. Shariffuddin, Polysulfide synthesis using waste cooking palm oil via inverse vulcanization, Chem. Eng. Technol. 45 (2022) 971–978, https://doi.org/10.1002/ceat.202100465.
[9] M.P. Crockett, A.M. Evans, M.J. Worthington, I.S. Albuquerque, A.D. Slattery, C. T. Gibson, J.A. Campbell, D.A. Lewis, G.J.L. Bernardes, J.M. Chalker, Sulfur-limonene polysulfide: a material synthesized entirely from industrial by-products and its use in removing toxic metals from water and soil, Angew. Chem. Int. Ed. 55 (2016) 1714–1718, https://doi.org/10.1002/anie.201508708.
[10] Z. Abo-Shanab, A.A. Altalhi, M. Noh, A.S. Mansour, M. Elshafie, U.F.M. Kandil, E. Azmy, An efficient ring-opening copolymerization of elemental sulfur with various olefinic compounds to produce thermoplastic polymeric sulfur: synthesis and characterization, Egypt. J. Chem. 66 (2023) 1967–1976, https://doi.org/10.21608/ejchem.2023.222372.8241.
[11] J.J. Griebel, N.A. Nguyen, S. Namnabat, L.E. Anderson, R.S. Glass, R.A. Norwood, M.E. Mackay, K. Char, J. Pyun, Dynamic covalent polymers via inverse vulcanization of elemental sulfur for healable infrared optical materials, ACS Macro Lett. 4 (2015) 862–866, https://doi.org/10.1021/acsmacrolett.5b00502.
[12] A.G. Simmonds, J.J. Griebel, J. Park, K.R. Kim, W.J. Chung, V.P. Oleshko, J. Kim, E.T. Kim, R.S. Glass, C.L. Soles, Y-E. Sung, K. Char, J. Pyun, Inverse vulcanization

of elemental sulfur to prepare polymeric electrode materials for Li–S batteries, ACS Macro Lett. 3 (2014) 229–232, https://doi.org/10.1021/mz400649w.
[13] J. Xiao, Z. Liu, W. Zhang, N. Deng, J. Liu, F. Zhao, Inverse vulcanization of a natural monoene with sulfur as sustainable electrochemically active materials for lithium-sulfur batteries, Molecules 26 (2021) 7039, https://doi.org/10.3390/molecules26227039.
[14] D.J. Parker, S.T. Chong, T. Hasell, Sustainable inverse-vulcanised sulfur polymers, RSC Adv. 8 (2018) 27892–27899, https://doi.org/10.1039/C8RA04446E.
[15] A. Gupta, M.J. Worthington, H.D. Patel, M.R. Johnston, M. Puri, J.M. Chalker, Reaction of sulfur and sustainable algae oil for polymer synthesis and enrichment of saturated triglycerides, ACS Sustain. Chem. Eng. 10 (2022) 9022–9028, https://doi.org/10.1021/acssuschemeng.1c08139.
[16] P.Y. Sauceda-Oloño, B.G. Guinati, A.D. Smith, R.C. Smith, Influence of additives on flame-retardant, thermal, and mechanical properties of a sulfur–triglyceride polymer composite, J. Compos. Sci. 8 (2024) 304, https://doi.org/10.3390/jcs8080304.
[17] Z. Huang, Y. Deng, D.H. Qu, Adding value into elementary sulfur for sustainable materials, Chem. Eur. J. 31 (2025) e202500125, https://doi.org/10.1002/chem.202500125.
[18] D. Choi, Y. Lee, Z.H. Lin, S. Cho, M. Kim, C.K. Ao, et al., Recent advances in triboelectric nanogenerators: from technological progress to commercial applications, ACS Nano 17 (2023) 11087–11219, https://doi.org/10.1021/acsnano.2c12458.
[19] C.H. Li, X. Ma, J. Fu, Y. Sun, F. Wang, Z. Huang, J. Li, Advanced materials for triboelectric nanogenerator, J. Phys. D Appl. Phys. 56 (2023) 394001, https://doi.org/10.1088/1361-6463/acdd0c.
[20] F.R. Fan, W. Tang, Z.L. Wang, Flexible nanogenerators for energy harvesting and self-powered electronics, Adv. Mater. 28 (2016) 4283–4305, https://doi.org/10.1002/adma.201504299.
[21] A. Yu, M. Song, Y. Zhang, Y. Zhang, L. Chen, J. Zhai, Z.L. Wang, Self-powered acoustic source locator in underwater environment based on organic film triboelectric nanogenerator, Nano Res. 8 (2015) 765–773, https://doi.org/10.1007/s12274-014-0559-z.
[22] G.M. Rani, C.M. Wu, K.G. Motora, R. Umapathi, Waste-to-energy: utilization of recycled waste materials to fabricate triboelectric nanogenerator for mechanical energy harvesting, J. Clean. Prod. 363 (2022) 132532, https://doi.org/10.1016/j.jclepro.2022.132532.
[23] S.M. Nawaz, M. Saha, N. Sepay, A. Mallik, Energy-from-waste: a triboelectric nanogenerator fabricated from waste polystyrene for energy harvesting and self-powered sensor, Nano Energy 104 (2022) 107902, https://doi.org/10.1016/j.nanoen.2022.107902.
[24] G. Han, B. Wu, Y. Pu, A triboelectric nanogenerator based on waste plastic bags for flexible vertical interconnection system, Microsyst. Technol. 26 (2020) 3893–3899, https://doi.org/10.1007/s00542-020-04879-6.
[25] P. Slobodian, R. Olejnik, J. Matyas, P. Riha, B. Hausnerova, A coupled piezo-triboelectric nanogenerator based on the electrification of biaxially oriented polyethylene terephthalate food packaging films, Nano Energy 118 (2023) 108986, https://doi.org/10.1016/j.nanoen.2023.108986.
[26] R. Stepancikova, R. Olejnik, J. Matyas, M. Masar, B. Hausnerova, P. Slobodian, Pressure-driven piezoelectric sensors and energy harvesting in biaxially oriented polyethylene terephthalate film, Sensors 24 (2024) 1275, https://doi.org/10.3390/s24041275.
[27] P. Slobodian, P. Riha, B. Hausnerova, Unsorted postconsumer plastic waste in energy conversion using piezoelectric, triboelectric, and pyroelectric generation mechanisms, ACS Sustainable Chem. Eng. 13 (2025) 2683–2693, https://doi.org/10.1021/acssuschemeng.4c06984.
[28] P. Slobodian, B. Hausnerova, P. Riha, V. Pata, R. Olejnik, J. Matyas, Turning plastic waste immiscibility into an advantage: efficiency improvement of PVDF-based energy harvesters using post-consumer thermoplastics, Adv. Mater. Interfaces 12 (2025) 2500070, https://doi.org/10.1002/admi.202500070.
[29] J.H. Lee, K.H. Kim, M. Choi, J. Jeon, H.J. Yoon, J. Choi, Y.S. Lee, M. Lee, J.J. Wie, Rational molecular design of polymeric materials toward efficient triboelectric energy harvesting, Nano Energy 66 (2019) 104158, https://doi.org/10.1016/j.nanoen.2019.104158.
[30] J. Choi, S. Won, H.J. Yoon, J.H. Lee, H.W. Jang, J. Jeon, A.Y. Kim, S.H. Park, J. H. Youk, M. Lee, J.J. Wie, Toxic gas-free synthesis of extremely negative triboelectric sulfur copolymer blends via phase separation of fluorine-rich polymers, Nano Energy 92 (2022) 106761, https://doi.org/10.1016/j.nanoen.2021.106761.
[31] W. Cho, S. Kim, H. Lee, N. Han, H. Kim, M. Lee, T.H. Han, J.J. Wie, High-performance yet sustainable triboelectric nanogenerator based on sulfur-rich polymer composite with MXene segregated structure, Adv. Mater. 36 (2024) 2404163, https://doi.org/10.1002/adma.202404163.
[32] W. Cho, S. Kim, J.J. Wie, Value-addition of wastes from petroleum refining process: sulfur-rich polymers for sustainable and high-performance optical and energy applications, Accounts Mater. Res. 5 (2024) 625–639, https://doi.org/10.1021/accountsmr.4c00039.
[33] S.A. Basith, G. Khandelwal, D.M. Mulvihill, A. Chandrasekhar, Upcycling of waste materials for the development of triboelectric nanogenerators and self-powered applications, Adv. Funct. Mater. 34 (2024) 2408708, https://doi.org/10.1002/adfm.202408708.
[34] K.U. Kumar, S. Hajra, G. Mohana Rani, S. Panda, R. Umapathi, S. Venkateswarlu, H.J. Kim, Y.K. Mishra, R.R. Kumar, Revolutionizing waste-to-energy: harnessing the power of triboelectric nanogenerators, Adv. Compos. Hybrid Mater. 7 (2024) 91, https://doi.org/10.1007/s42114-024-00903-9.
[35] P. Jaiban, S. Khumtrong, P. Kongchana, T. Theethuan, S. Lokakaew, P. Phutthami, A. Watchrapasorn, R. Guo, A.S. Bhalla, The biofilm from soybean meal for application in triboelectric generator, Mater. Lett. 325 (2022) 132862, https://doi.org/10.1016/j.matlet.2022.132862.
[36] L.S. Vikram, S. Potu, D.P. Kasireddi AK, U.K. Khanapuram, H. Divi, R.K. Rajaboina, Biowaste sea shells-based triboelectric nanogenerator: sustainable approach for efficient mechanical energy harvesting, Energy Technol. 13 (2025) 2401333, https://doi.org/10.1002/ente.202401333.
[37] Q.M. Saqib, R.A. Shaukat, M.U. Khan, M. Chougale, J. Bae, Biowaste peanut shell powder-based triboelectric nanogenerator for biomechanical energy scavenging and sustainably powering electronic supplies, ACS Appl. Electron. Mater. 2 (2020) 3953–3963, https://doi.org/10.1021/acsaelm.0c00791.
[38] J.M. Wu, C.K. Chang, Y.T. Chang, High-output current density of the triboelectric nanogenerator made from recycling rice husks, Nano Energy 19 (2016) 39–47, https://doi.org/10.1016/j.nanoen.2015.11.014.
[39] S.A. Graham, B. Dudem, A.R. Mule, H. Patnam, J.S. Yu, Engineering squandered cotton into eco-benign microarchitectured triboelectric films for sustainable and highly efficient mechanical energy harvesting, Nano Energy 61 (2019) 505–516, https://doi.org/10.1016/j.nanoen.2019.04.081.
[40] H. Varghese, A. Chandran, Triboelectric nanogenerator from used surgical face mask and waste mylar materials aiding the circular economy, ACS Appl. Mater. Interfaces 13 (2021) 51132–51140, https://doi.org/10.1021/acsami.1c16557.
[41] M. Navaneeth, S. Potu, A. Babu, B. Lakshakoti, R.K. Rajaboina, K.U. Kumar, D. Haranath, P. Kodali, K. Balaji, Transforming medical plastic waste into high-performance triboelectric nanogenerators for sustainable energy, health monitoring, and sensing applications, ACS Sustain. Chem. Eng. 11 (2023) 12145–12154, https://doi.org/10.1021/acssuschemeng.3c03136.
[42] M. Sahu, S. Hajra, H.G. Kim, H.G. Rubahn, Y.K. Mishra, H.J. Kim, Additive manufacturing-based recycling of laboratory waste into energy harvesting device for self-powered applications, Nano Energy 88 (2021) 106255, https://doi.org/10.1016/j.nanoen.2021.106255.
[43] M.Y. Chougale, Q.M. Saqib, M.U. Khan, R.A. Shaukat, J. Kim, D. Dubal, J. Bae, Expired pharmaceutical drugs as tribopositive material for triboelectric nanogenerator, Adv. Sustainable Syst. 5 (2021) 2100205, https://doi.org/10.1002/adsu.202100205.
[44] M. Navaneeth, S. Potu, A. Babu, R.K. Rajaboina, U. Kumar, H. Divi, P. Kodali, A medical waste X-ray film based triboelectric nanogenerator for self-powered devices, sensors, and smart buildings, Environ. Sci. Adv. 2 (2023) 848–860, https://doi.org/10.1039/d3va00018d.
[45] V.L. Sunitha, P. Supraja, K.D. Prasad, M. Navaneeth, A. Babu, V. Mahesh, K. U. Kumar, D. Haranath, R.R. Kumar, Wood plastic composites (WPC) waste based triboelectric nanogenerator for mechanical energy harvesting and self-powered applications, Mater. Lett. 351 (2023) 134995, https://doi.org/10.1016/j.matlet.2023.134995.
[46] M.Y. Chougale, Q.M. Saqib, M.U. Khan, R.A. Shaukat, J. Kim, J. Bae, Novel recycled triboelectric nanogenerator based on polymer-coated trash soda can for clean energy harvesting, Adv. Sustainable Syst. 5 (2021) 2100161, https://doi.org/10.1002/adsu.202100161.
[47] A. Kaki, G. Maharana, N. Madathil, V. Mahesh, K.U. Kumar, P.J. Daniel, R. K. Rajaboina, Electronic waste to energy: self-powered electronic devices and organic dye degradation using TENG-assisted photocatalysis, Adv. Sustainable Syst. 9 (2025) e00235, https://doi.org/10.1002/adsu.202500235.
[48] V.L. Suneetha, V. Mahesh, P. Supraja, M. Navaneeth, K.K. Uday, R.R. Kumar, Facile and robust high-performance triboelectric nanogenerator based on electronic waste for self-powered electronics, Energ. Technol. 13 (2025) 2401387, https://doi.org/10.1002/ente.202401387.
[49] A. Šutka, K. Mālnieks, L. Lapčinskis, M. Timusk, K. Kalniņš, A. Kovaļovs, J. Bitenieks, M. Knite, D. Stevens, J. Grunlan, Contact electrification between identical polymers as the basis for triboelectric/flexoelectric materials, Phys. Chem. Chem. Phys. 22 (2020) 13299–13305, https://doi.org/10.1039/D0CP01947J.
[50] A. Šutka, P.C. Sherrell, N.A. Shepelin, L. Lapčinskis, K. Mālnieks, A.V. Ellis, Measuring piezoelectric output—fact or friction? Adv. Mater. 32 (2020) 2002979 https://doi.org/10.1002/adma.202002979.
[51] J. Zhang, C. Boyer, Y.X. Zhang, Enhancing the humidity resistance of triboelectric nanogenerators: a review, Small 20 (2024) 2401846, https://doi.org/10.1002/smll.202401846.
[52] https://www.icdd.com ICDD – International Centre for Diffraction Data, PDF No. 00–008-0247: Sulfur, Orthorhombic. Newtown Square, PA, USA. (accessed on July 15, 2025), 2025.
[53] L.M. Rovatta, R.E. de Prada, M.M. Bruno, D.F. Acevedo, G.A. Monti, Structure–property relationships and mechanical performance of inverse vulcanized sulfur-soybean oil polymer films and their biochar-reinforced biocomposites, ACS Appl. Polym. Mater. 7 (2025) 15316–15328, https://doi.org/10.1021/acsapm.5c02739.
[54] A.S. Farioli, M.V. Martinez, C. Barbero, E. Yslas, D. Acevedo, The effect of oil raw material composition in the synthesis of bio-sorbents based on inverse vulcanization on the ability to remediate hydrocarbon-contaminated water. A novel method for decontaminating water/fuel emulsions, J. Appl. Polym. Sci. 141 (2024) e54914, https://doi.org/10.1002/app.54914.
[55] P.Y. Sauceda-Oloño, C.V. Lopez, B.K. Patel, A.D. Smith, R.C. Smith, Influence of thermal and chemical stresses on thermal properties, crystal morphology, and mechanical strength development of a sulfur polymer composite, Macromolecules (2024) 240–252, https://doi.org/10.3390/macromol4020013.
[56] Y. Liu, W. Liu, Z. Wang, W. He, Q. Tang, Y. Xi, X. Wang, H. Guo, C. Hu, Quantifying contact status and the air-breakdown model of charge-excitation triboelectric

nanogenerators to maximize charge density, Nat. Commun. 11 (1) (2020) 1599, https://doi.org/10.1038/s41467-020-15368-9.
[57] W.G. Kim, D.W. Kim, I.W. Tcho, J.K. Kim, M.S. Kim, Y.K. Choi, Triboelectric nanogenerator: structure, mechanism, and applications, ACS Nano 15 (2021) (2021) 258–287, https://doi.org/10.1021/acsnano.0c09803.
[58] U.G. Musa, S.D. Cezan, B. Baytekin, H.T. Baytekin, The charging events in contact-separation electrification, Sci. Rep. 8 (2018) 2472, https://doi.org/10.1038/s41598-018-20413-1.
[59] P.K. Yang, Z.H. Lin, K.C. Pradel, L. Lin, X. Li, X. Wen, H. He, Z.L. Wang, Paper based origami triboelectric nanogenerators and self-powered pressure sensors, ACS Nano 9 (2015) 901–907, https://doi.org/10.1021/acsomega.9b01963.
[60] T. Kamilya, P.K. Sarkar, S. Acharya, Unveiling peritoneum membrane for a robust triboelectric nanogenerator, ACS Omega 4 (2019) 17684–17690, https://doi.org/10.1021/nn506631t.
[61] T. Jin, Z. Sun, L. Li, Q. Zhang, M. Zhu, Z. Zhang, G. Yuan, T. Chen, Y. Tian, X. Hou, C. Lee, Triboelectric nanogenerator sensors for soft robotics aiming at digital twin applications, Nat. Commun. 11 (2020) 5381, https://doi.org/10.1038/s41467-020-19059-3.